Ph. D. DISSERTATION

Generation of finite power Airy beams based on holographic and plasmonic approaches

홀로그래피와 플라즈모닉스에 기반한 에어리 빔 생성

BY

DAWOON CHOI

FEBRUARY 2014

DEPARTMENT OF ELECTRICAL AND
COMPUTER ENGINNERING
COLLEGE OF ENGINEERING
SEOUL NATIONAL UNIVERSITY

Abstract

Generation of finite power Airy beams based on holographic and plasmonic approaches

DAWOON CHOI
DEPARTMENT OF ELECTRICAL AND COMPUTER ENGINEERING
COLLEGE OF ENGINEERING
SEOUL NATIONAL UNIVERSITY

An Airy beam is a kind of non-diffracting wave such as Bessel beam and Weber beam, which keeps its initial field profile during propagation. It was theoretically analyzed by Berry and Balazs as a non-trivial solution of the Schrödinger equation describing movements of a free particle under the free-potential condition. Until now, the Airy beam has attracted much attention due to their three representative characteristics: *non-diffraction*, *free-acceleration* and *self-healing*. First, an Airy beam has the invariant field profile during propagation: non-diffraction. Second, the Airy beam has the unique bending trajectory without any external force: free-acceleration. Lastly, the Airy beam has the ability to reconstruct its original shape after being partially blocked by an opaque obstacle: self-healing. These properties can be understood by noticing that a number of straight rays form the parabolic caustic. However, it is impossible to experimentally build up an Airy beam since it has a long tail containing infinite power. Thus, a finite power Airy beam was introduced by suppressing side lobes of an ideal Airy beam.

Although this Airy-like beam cannot remain the non-diffraction feature permanently, it shows not only reasonable propagation length with keeping its Airy field profile but also distinguished properties such as both free-acceleration and a self-healing ability.

In this dissertation, the generation method of the finite power Airy beams via initial field modulation to suppress side lobes is presented. Three types of input beam cases, which are a Gaussian beam, a uniform beam of finite extent and an inverse Gaussian beam, are investigated both theoretically and experimentally. Especially, the finite power Airy beam generated by a uniform input beam of finite extent retains the Airy field profile much longer than that of the Airy beam generated by a conventional Gaussian beam. Also, the finite power Airy beams generated by an inverse Gaussian input beam forms a unique focused-bending beam.

To generate the finite power Airy beams, a novel method based on holography which is the recording and reconstruction technique of optical fields including amplitude and phase information, is introduced. After interference patterns of a reference beam and a finite power Airy beam are recorded on a photopolymer, the finite power Airy beams can be regenerated by simply illuminating the reference beam on the hologram. In addition, using the characteristics of holography, the self-healing property and more bended propagation of the reconstructed Airy beams are experimentally verified. Moreover, angle multiplexing of the multiple Airy beams determined by the angles of the reference beams is presented. This might enable the parallel processing of particle manipulations using the Airy beams.

A new method to launch the finite power Airy beams based on the metallic slit array is presented. By tailoring the amplitude and phase of the transmitted fields from the metallic slit array, the launching of Airy beam with compact area has been achieved in free space. From the Huygens' principle, diffracted light at the slit end acts individual point sources and forms the interference patterns by controlling surface plasmon polartons (SPPs) diffracted at the exit of the subwavelength slit. It is expected that this method is used to various applications like particle tweezing, sorting, clearing and trapping without any optical components and bulky structure.

Keywords: Airy beams, Airy beam generation, finite power Airy beams, holography, angle multiplexing based on holography, surface plasmons, plasmonics, metal-insulator-metal waveguide, subwavelength slit, plasmonic lens, beam pattern generation

Student number: 2010-30233

Contents

List of Figures

Chapter 1.

Introduction

1.1. Overview of Airy beams

In 1978 Berry and Balazs first introduced the non-spreading wave packet from the Schrödinger equation in quantum mechanics for a free particle [1]. The Airy wave packet is the only non-trivial solution which has following unique properties: non-spreading according to time varying and free-acceleration without any external potential.

From the paraxial Helmholtz equation which mathematically correspondents to the Schrödinger equation, in 2007, Siviloglou and Christodoulides showed the optical version of the Airy wave packet, namely Airy beams [2]. The Airy beam is a kind of non-diffraction beams whose transverse intensity distributions are assumed by Airy functions shown in the inset of Fig. 1.1. They presented the Airy beam solutions in one dimension (1D or (1+1)D) and two dimension (2D or (2+1)D) adopting an exponentially decaying aperture. This work led experimental realizations of *finite power* Airy beams because ideal Airy beams are not square integrable (i. e., they convey infinite power) [3]. Understandably, presented finite power Airy beams have the similar characteristics with that of the Airy wave packet - non-diffraction during propagation and the bending trajectory without any external force or any refractive index gradient as shown in Fig. 1.1. Also, just like other non-diffraction beams, it was reported that they have the self-healing phenomenon which is restoring their original shapes despite blocking a part of whole beams [4,5].

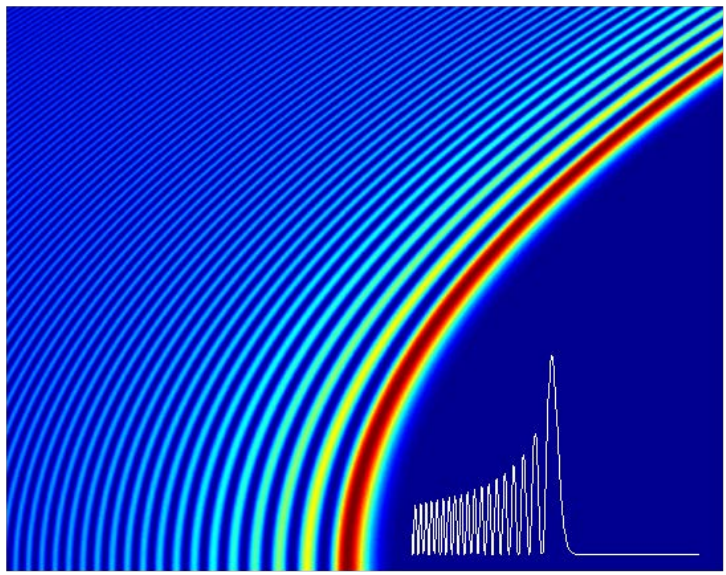

Figure 1.1 Intensity distribution of (1+1)D ideal Airy beams. During propagation, an Airy profile is invariant (non-diffraction) and the intensity maximum is moving along a bending trajectory (free-acceleration). An inset is a transverse cross-section plot at the origin. It shows an Airy function profile.

Surface plasmon polariton (SPP) is an electromagnetic wave that propagates along a metal-dielectric interface as shown in Fig. 1.2 [6, 7]. Let me consider a basic geometry sustaining SPPs, which is a single interface between a dielectric medium with dielectric constant ε_d and a flat metal with permittivity ε_m in a transverse magnetic (TM) case. In a dielectric medium ($z \geq 0$), the electromagnetic fields can be expressed by the Maxwell's curl equation:

$$H_y(z) = A_1 \exp(i\beta x - k_d z), \tag{1.1}$$

$$E_x(z) = i\frac{A_1}{\omega\varepsilon_0\varepsilon_d} k_d \exp(i\beta x - k_d z), \tag{1.2}$$

and

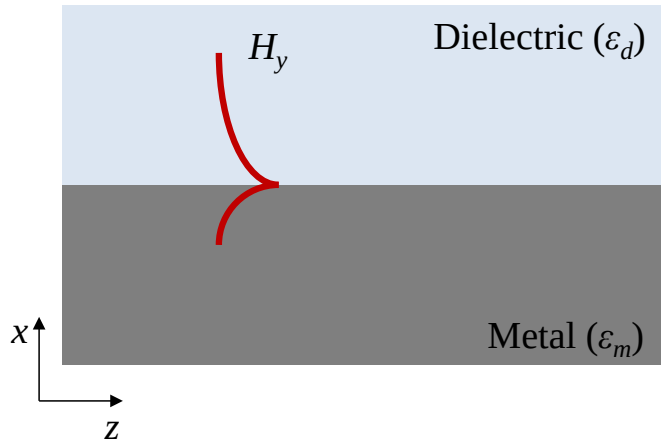

Figure 1.2 Propagation of surface plasmon polariton at the interface between a metal and a dielectric medium.

$$E_z(z) = -A_1 \frac{\beta}{\omega \varepsilon_0 \varepsilon_d} \exp(i\beta x - k_d z), \tag{1.3}$$

where β is a propagation constant of an SPP wave and k_d is the wavevector in the x-direction. In similar manner, in a metal ($z < 0$), the electromagnetic fields can be expressed by

$$H_y(z) = A_2 \exp(i\beta x + k_m z), \tag{1.4}$$

$$E_x(z) = -i \frac{A_2}{\omega \varepsilon_0 \varepsilon_m} k_m \exp(i\beta x + k_m z), \tag{1.5}$$

and

$$E_z(z) = -A_2 \frac{\beta}{\omega \varepsilon_0 \varepsilon_m} \exp(i\beta x + k_m z), \tag{1.6}$$

where k_m is the wavevector in the perpendicular direction to the interface. A_1 and A_2 denote coupling coefficients. From the continuity relations, the dispersion relation for the SPP wave is

$$\beta = k_0 \sqrt{\frac{\varepsilon_d \varepsilon_m}{\varepsilon_d + \varepsilon_m}}, \tag{1.7}$$

where k_0 (=ω/c) is the wavevector in free space. This field is strongly confined beyond diffraction limit and exponentially decayed in a transverse direction from the metal surface. As a result, hundreds or thousands of times field enhancements can be achieved in subwavelength structures [8-12]. Using this characteristic, various applications such as imaging, lithography, sensor and optical data storage have been actively reported [13-20]. However, intrinsic metallic loss due to internal damping of a metal is inevitable. Hence, it becomes an obstacle to practical use of nano-metallic structures based on SPP. Here, SPP wavelength λ_{SPP} is defined by

$$\lambda_{SPP} = \frac{2\pi}{\mathrm{Re}(\beta)}. \tag{1.8}$$

Recently, *Airy plasmon* is presented as a promising candidate to solve confronting hurdles of SPP [21-28]. Following respects of Airy plasmon are easy to adopt in a practical planar metallic system. Firstly, it shows relatively long propagation length than that of other non-diffraction beams on the metal surface. Secondly, since the origin of Airy beams is a superposition of plane waves in free space, it can be replaced with SPP waves in a metal surface. Thirdly, in general, it is difficult to express non-diffraction beams such as Bessel beams and parabolic beams in a plane because more than one coordinates are essential. On the contrary, Airy beams even have a quasi-one-dimensional form such as (1+1)D or (2+1)D. Finally, it is not sensitive to surface roughness or defects because of their self-healing property.

The first optical observation of the Airy beams was realized by the optical Fourier transform system shown in Fig. 1.2 which is adding the cubic phase to a broad Gaussian beam. After a computer-generated phase mask on a spatial light modulator (SLM) is illuminated by an input Gaussian beam, inverse Fourier transform is performed by a Fourier lens. As a result, the Airy beams are generated at the image plane. [3]. On the same principle, observations of Airy beams in wide area such as nonlinear generation [29-31], curved plasma channel generation [32] and electron beam generation [33] were reported. Meanwhile, to couple a plane wave in free space into SPPs on a metal surface, there are two representative methods such as prism coupling and grating coupling which

compensate a lack of *k*-vector of the plane wave in free space [34]. Recently, using a grating coupling method, another way to generate Airy beams on a metal surface which directly assigns initial launching conditions was suggested by Minovich *et al*. [22, 30]. For matching initial intensity and phase distributions of Airy beams, grating width in a *x*-direction is proportional to intensity distributions of Airy beams and grating position is determined according to SPP wavelength. Adjacent grating is positioned with a π-phase difference of SPP wavelength. They used a 10 mW CW diode laser with 784 nm wavelength. A period of the *z*-direction is 764 nm, which is equal to SPP wavelength at 784 nm. Overall size of the structure is approximately 20 μm × 10 μm. Figure 1.3(a) is a scanning electron microscope (SEM) image of a designed grating array on a gold film with a 150 nm thickness, which is fabricated by a focused ion beam (FIB). In this case, the permittivity of gold is -10.5099+1.0573*i* at 660 nm wavelength and 628 nm of SPP wavelength is calculated by Eq. (1.8). 100 nm of grating width in the *y*-direction is fixed. While a laser beam of 660 nm wavelength is illuminating the sample at the bottom, Airy plasmons ((1+1)D Airy beams) measured by a near-field scanning optical microscope (NSOM) are excited at a gold surface shown in Fig. 1.3(b). Also, Li *et al*. presented an array structure for launching plasmonic Airy beams based on in-plane diffractions [23]. When SPPs propagate through graded diffraction gratings (from 420 nm to 780 nm with 10 nm increment) on a 60-nm-thickness silver film, they are scattered by these designed nanocave array. As a result, interference patterns (Airy plasmons) are formed according to the Huygens-Fresnel principle. They excited SPPs using a He-Ne laser with 632.8 nm wavelength. They experimentally demonstrated the self-healing property of the Airy plasmons and recorded them using a leakage radiation microscopy (LRM) system. Last, Zhang *et al*. suggested a new technique to launch plamonic Airy beams [25]. Using the grating coupler with a 805 nm period on a 50m-thickness gold surface, cubic phase modulated beams with 820 nm wavelength were coupled into Airy plasmons after passing through a objective lens. They dynamically controlled trajectories of Airy plasmons by controlling the transverse or longitudinal positions of the objective lens or changing the phase mask on the SLM. Observation of Airy plasmons was conducted by the LRM system which shows real time images of Airy plasmons.

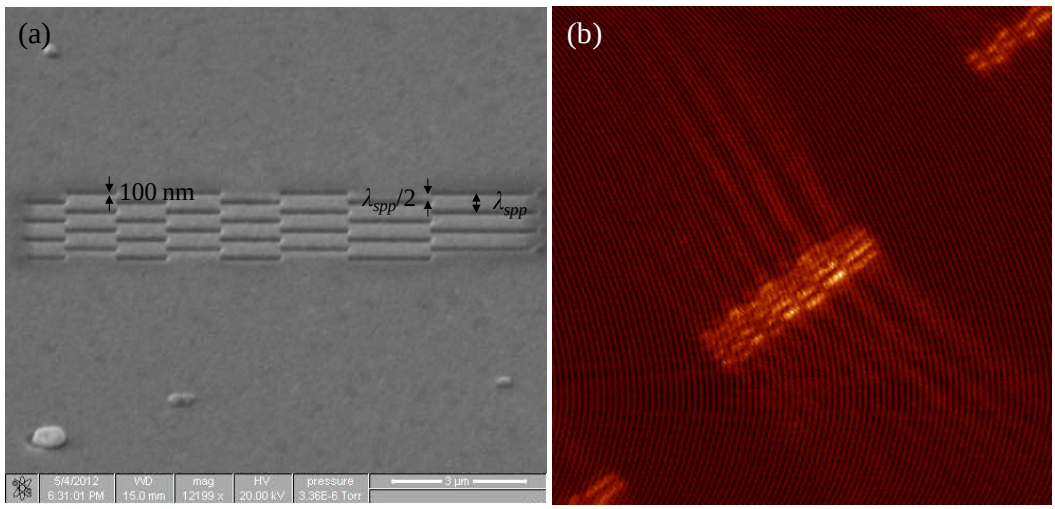

Figure 1.3 (a) SEM image of a fabricated slit array for exciting Airy plasmons. (b) Intensity distribution of Airy plasmons measured by the NSOM system.

1.2. Motivation of this dissertation

To resolve the problem that ideal Airy beams are not square integrable (i.e., they carry infinite power), exponentially decaying terms were introduced to implement finite power Airy beams [2], which have similar features to those of the ideal one. They were generated by the optical Fourier transform of a Gaussian input beam on which cubic phase is imposed [3]. Although they can carry finite power, these *apodized* finite power Airy beams cannot maintain their shapes for a long time and are gradually spreading out during propagation [3]. Recently, based on these, various methods which tune a main lobe or side lobes of finite power Airy beams by using a flat-topped input Gaussian beam [35], a nonsymmetric apodization [36] and a sharp cutoff [37] were presented.

In this dissertation, some alternative methods for the apodization of Airy beams for solving a diffraction issue in finite power Airy beams are presented [38]. Instead of Gaussian input beams (that involve exponentially decaying terms), uniformly distributed beams of finite extent or beams having an inverse Gaussian distribution is considered. In the case of a uniformly distributed finite-extent beam, it shows that the resultant finite

power Airy beam can preserve its Airy profile much farther than that generated by the Gaussian input beam. An inverse Gaussian apodization results in a unique propagation dynamics: a focused-bending beam. In each case, the solution of the finite power Airy beam is derived and verified by experiments. This work will provide not only the effects of initial fields in finite power Airy beams but also the method to overcome the diffraction problem in non-diffraction beams with finite power.

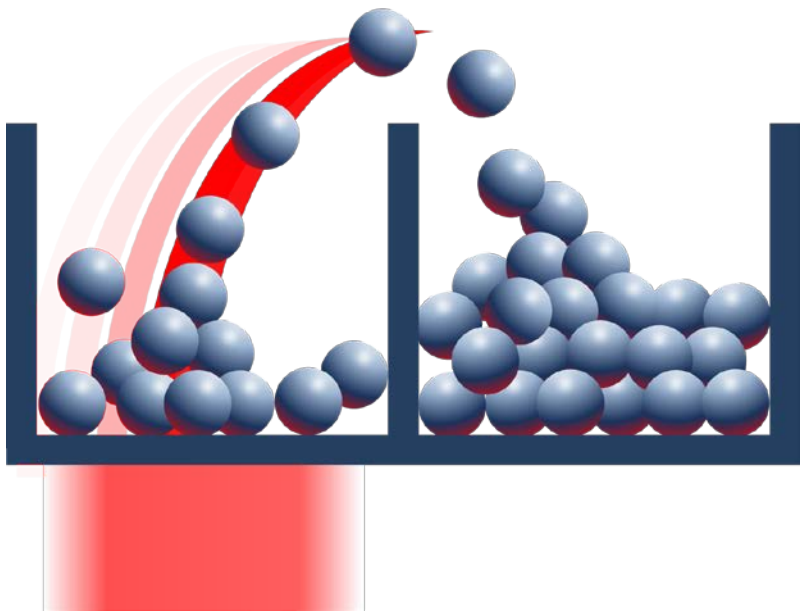

Figure 1.4 Concept of optically mediated particle clearing along a bending trajectory of Airy beams.

Recently, using an unique bending property of Airy beams, optically mediated particle clearing was experimentally demonstrated [4,39-42]. Using (2+1)D Airy beams with an Ar+ laser of 514 nm wavelength and 25 mW power, colloidal glass spheres of 1.5 μm diameter were conveyed from one section to another section along parabolic trajectories shown in Fig. 1.4 [4]. Also, an optical tweezer system was reported based on the optical trapping force of the focused Airy beams [40]. When a 532 nm laser with 5 W peak power illuminates polymer particles with 3.2 μm diameter diffused in de-ionized water, optical trapping takes place before the focus, at the focus and after the focus. Optical tweezers use so-called gradient force of the electric field of a highly focused laser

beam to manipulate nano- or micro-size dielectric particles without physical contact [43-48]. They are useful in sorting or guiding cells, molecules and DNAs in a biological system. In optical tweezers, there are several important things to consider: (1) improvements in spatial- and time-resolutions and (2) removals of experimental noise such as temperature drift, mechanical and acoustic vibrations and background electronic noise. In addition, multiple optical trapping is very useful because it can allow parallel processing of simultaneous particle manipulations. Especially, based on holographic method using an SLM or a diffractive optical element (DOE), simultaneous operations are possible to achieve the high throughput [47,48].

In this dissertation, holographic generations of Airy beams in the beginning are demonstrated. By recording and reconstruction of holograms which consist of the interference between generated Airy beam using the optical Fourier transform system and a plane wave, decoded Airy beams have non-diffracted nature with a bending trajectory [49]. After that, multiplexing operations of two Airy beams (accelerations in opposite directions) determined by the angles of reference beams are presented. In addition, based on the characteristics of holography, the self-healing property and the conjugated Airy beams are investigated. This approach can be utilized to not only a novel and robust Airy beam generation method but also an optical tweezing system with multiplexing of Airy beams.

To generate the Airy beam in free space, a method of cubic-phase wrapping to a Gaussian beam has been used typically [3]. After passing through an optical Fourier transform system which consists of the phase mask with a cubic-phase modulation placed one focal length in front of a lens, the incident Gaussian beam is transformed into the finite power Airy beams in the Fourier plane placed one focal length behind the lens. Also, a frequency converted Airy beams based on nonlinear processes and a femto-second Airy beams in curved plasma channel have been generated by the same method [29-32]. However, these methods are not appropriate for applying to the compact-sized system because the bulky optical devices of high-cost such as femto-second lasers, SLMs and several optical elements should be required. Meanwhile, it is already known that both fast transmission speed and broadband communication processes can be achieved

by light. However, due to inevitable nature of light, namely diffraction limit which causes no observation below subwavelength, light remained just one of candidates to solve urgent issues of electronics such as slow operation speed and bulky size reduction. Recently, however, growing with remarkable developments of the manufacturing technology leads developments of the nanotechnology. Especially, plasmonics which combines SPPs and nanostructures is widely researched on nano-imaging, nano-lithography, nano-manufacturing and so on.

In this dissertation, a new method to generate Airy beams in free space based on plasmonics is proposed [50]. After an SPP wave is passing through subwavelength slit, it is coupled to a spherical wave in free space. Since each spherical wave can be regarded as an individual point source from the Huygens' principle, arbitrary interference pattern generations are possible. According to this phenomenon, a subwavelength slit array to manipulate light caustics which are satisfied to a Airy beam trajectory is designed. The designed structure, so-called metallic lens, acts as combinations of an SLM and a lens. It shows that the generated Airy beams have the same properties such as non-diffraction, bending and self-healing as those of ideal Airy beams. This work enables to reduce overall size of an Airy beam generation system. Therefore, it can be utilized to various light manipulations as well as signal processing in optical integrated circuits.

1.3. Scope and organization

Unique natures (non-diffraction, bending trajectory and self-healing) of Airy beams have attracted much interest in optical science. To maintain these characteristics over a whole range, conserving an entire beam profile originated from infinity power is necessary. However, it is impossible to impose infinity power to Airy beams due to a realistic constraint. Therefore, practical approaches in Airy beam generation were attempted considering finite experimental environments such as finite power of laser source and finite size of optical elements.

In Chapter 2, I explain how to generate Airy beams in finite environments first and then present the effects originated from initial field modulations. In Section 2.1, I discuss

theoretical analysis of the Airy beams from the paraxial Helmholtz equation with potential-free. At first, the solutions of the ideal Airy beam and the finite power Airy beams are presented. From there, three types of apodization methods of ideal Airy beams are compared under the experimental conditions. In addition, dimension extension to the finite power Airy beams, which are the (2+1)D finite power Airy beams, is covered. In Section 2.2, the generation of the finite power Airy beams to three cases is experimentally observed. I provide the experimental results according to three different apodization types. These experimental results coincide well with the theoretical expectations in section 2.1.

Chapter 3 shows the generation of the finite power Airy beams by holographic method. Holographic generation consists of two procedures which are recording and reconstruction. In Section 3.1, the recording process of the (2+1)D Airy beams is introduced. After recording a reference beam and the Airy beams generated by the convention generation method based on the optical Fourier transform and reconstructing them, holographic Airy beams is achieved. Especially, in the reconstruction procedure, the self-healing property and conjugated Airy beams are shown by illuminating an imperfect reference beam or a phase-conjugated reference beam. In Section 3.2, I present angle multiplexing of two Airy beams according to the angles of the reference beams for practical uses. This work also consists of two stages. The recording procedures are conducted twice to record two Airy beams having different trajectories. In the reconstruction procedures, the reconstructed Airy beams can be obtained both simultaneously and separately.

From the Huygens' principle, it was widely known that diffracted light becomes a point source of spherical waves which form a specific patterns. In Chapter 4, I adopt this principle to manipulate the finite power Airy beams using subwavelength slit array. Thus, the design process of a subwavelength metallic slit array is explained in Section 4.1. Since a subwavelength slit can be regarded as a metal-insulator-metal waveguide, the transmittance and the phase retardation of a surface plasmon mode according to the metallic slit parameters are analyzed. In Section 4.2, the proposed structure is numerically demonstrated by COMSOL Multiphysics based on the finite elements

method. In addition, I show a simulation result about self-healing which is an important property of Airy beams.

Finally, concluding remarks for this dissertation and summary are provided in Chapter 5.

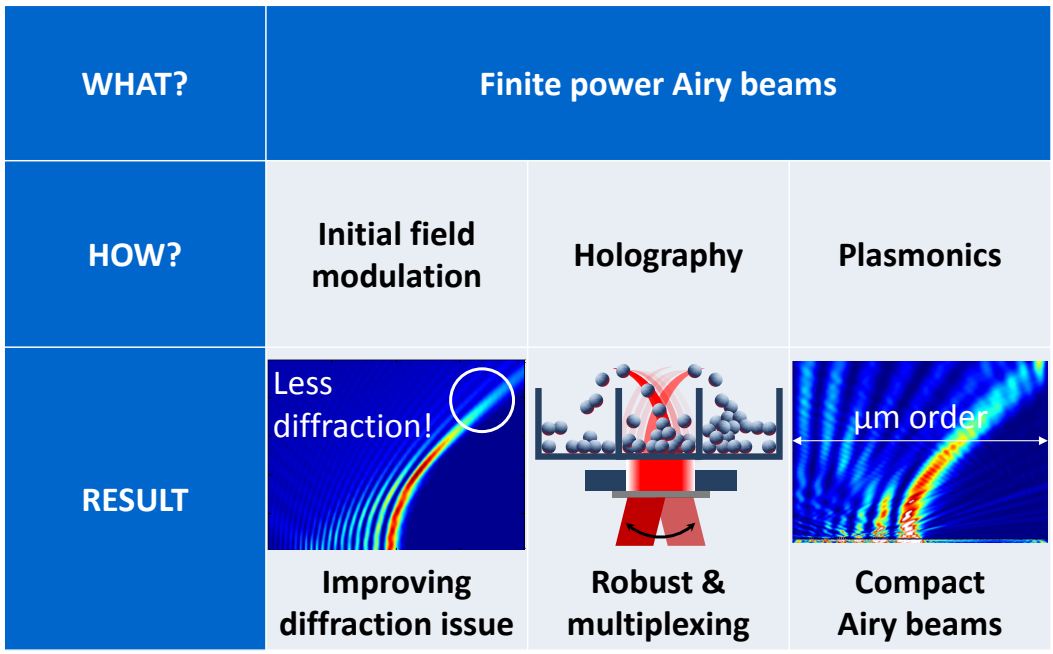

Figure 1.5 Scope of this dissertation.

Chapter 2.

Generation of Airy beams via initial field modulation

In this chapter, finite power Airy beams generated by the Fourier transform of a cubic phase-modulated beam of finite extent such as a Gaussian beam (*CASE* I), a uniform beam of finite extent (*CASE* II) and an inverse Gaussian beam (*CASE* III) are discussed. The propagation dynamics of resultant finite power Airy beams are analyzed and compared with three different input beam *CASES*. Both theoretical and experimental approaches show that the finite power Airy beam generated by the use of a uniform input beam (*CASE* II) retains the Airy profile much longer than the conventional finite power Airy beam (*CASE* I). Also, the finite power Airy beam via an inverse Gaussian beam (*CASE* III) builds up a focused-bending beam. It is expected that these works in this chapter can be utilized to particle manipulations such as sorting, tweezing and optical trapping.

2.1. Theoretical analysis of Airy beams

Since Berry and Balazs predicted the existence of non-spreading wave packets [1] and Siviloglou and Christodoulides studied their optical version [2], there have been very active researches on Airy beams [1-5, 21-33, 35-44, 49, 50, 54, 56-60]. To sum up their outcomes until now, three unique characteristics of Airy beams are presented. First, Airy beams are non-diffracting ones that satisfy the Helmholtz equation like Bessel [51] and parabolic beams [52]: *non-diffraction*. Second, Airy beams take up a bending trajectory

in homogeneous media without any external forces: *acceleration*. Lastly, Airy beams can recover their original shapes when a part of them is blocked by arbitrary obstacles: *self-healing*.

2.1.1. (1+1)D finite power Airy beams

The (1+1)D paraxial Helmholtz equation with potential-free (no gradient) can be written as

$$i\frac{\partial \phi}{\partial \xi}+\frac{1}{2}\frac{\partial^2 \phi}{\partial s^2}=0, \tag{2.1}$$

where ϕ is the electromagnetic wave function. s and ξ denote the transverse coordinate x scaled by an arbitrary scaling factor x_0 and the longitudinal coordinate z scaled by $k_n x_0^2$, respectively, where k_n ($=2\pi n/\lambda$) is a wavenumber in a propagating medium with a refractive index n, and λ is the wavelength of light in free space. By solving Eq. (2.1), the Airy beam solution ϕ can be obtained as follows [2]:

$$\phi_0(s,\xi)=\mathrm{Ai}\left(s-\left(\frac{\xi}{2}\right)^2\right)\exp\left(i\left(\frac{s\xi}{2}\right)-i\left(\frac{\xi^3}{12}\right)\right). \tag{2.2}$$

The Fourier transform Φ_0 of Eq. (2.2) at ξ=0 (at the initial position) is given by (Eq. (A.2))

$$\Phi_0(k)=\exp\left(i\frac{k^3}{3}\right). \tag{2.3}$$

As it was mentioned in the introduction, Eq. (2.3) is not square integrable and thus ϕ_0 is not physically realizable. Usually, an exponentially decaying function exp(as) is multiplied to ϕ_0 to obtain a finite power beam:

$$\phi_1(s,\xi=0)=\mathrm{Ai}(s)\exp(as), \tag{2.4}$$

which is square integrable and its Fourier transform Φ_1 becomes (Eq. (A.5))

$$\Phi_1(k)=\exp(-ak^2)\exp\left(\frac{i}{3}\left(k^3-3a^2k-ia^3\right)\right). \tag{2.5}$$

Based on Eq. (2.5) and its optical Fourier transform, the first observation of finite Airy beams was conducted: the cubic phase [$\exp\left(ik^3/3\right)$] was imposed on the Gaussian beam [$\exp(-ak^2)$] using a spatial light modulator (SLM) and the resultant, cubic phase-modulated Gaussian beam was Fourier transformed using a lens system [3]. If the higher-order terms of the relatively small constant a is ignored, $\exp\left(\frac{i}{3}(-3a^2k - ia^3)\right)$ in Eq. (2.5), the only difference between Eqs. (2.3) and (2.5) is the Gaussian function [$\exp(-ak^2)$] which is originated from the apodization, i.e., exponentially decaying term $\exp(as)$. Therefore, Eq. (2.3) can be understood as a plane wave (of infinite extent) with a cubic phase modulation, suggesting that the finite-extent feature of the input beam results in the finite power Airy beam.

2.1.2. Comparison with three *CASES* of Airy beams

This discussion, i.e., the fact that a finite power Airy beam can be generated by the Fourier transform of a cubic phase-modulated beam of finite extent, implies that there can be other methods for the apodization of ideal Airy beams. That is, other types of finite-extent beam than the Gaussian one can be used. Here, finite power Airy beams generated by three different input beams - those having a conventional Gaussian distribution (*CASE* I), a uniform distribution of finite extent (*CASE* II) and an inverse Gaussian distribution (*CASE* III) - are considered. At first, it is assumed that the wavelength of an incident beam λ is 633 nm, x_0 is 50 μm, the focal length of the lens f is 50 cm and the SLM has 1080 × 1080 pixels with an 8 μm pixel pitch.

First, let us start with the *CASE* I, which adopts a Gaussian beam as an input beam. Until now, there is no simulation including the experimental regime. Due to the finite size (modulation area) of the SLM, the incident Gaussian beam must be truncated. Therefore, Eq. (2.5) becomes

$$\Phi_1(k) = \Pi\left(\frac{\lambda f}{2\pi l}k\right)\exp(-ak^2)\exp\left(\frac{i}{3}\left(k^3 - 3a^2k - ia^3\right)\right), \tag{2.6}$$

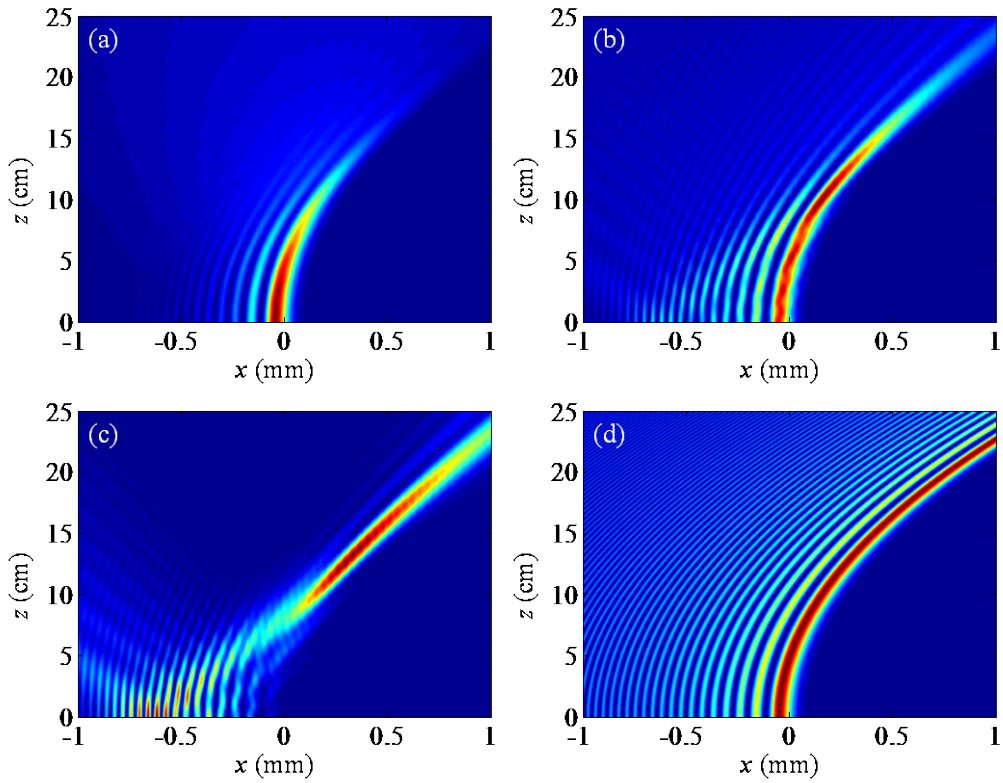

Figure 2.1 Propagation dynamics of finite power Airy beams generated by (a) a Gaussian beam, (b) a uniform beam of finite extent and (c) an inverse Gaussian beam. (d) Propagation dynamics of an ideal Airy beam.

where $\Pi(\alpha)$ is a rectangular function (1 if $|\alpha| < 0.5$ and 0 otherwise) and l is the length of the SLM along the one dimension given by the product of the pixel pitch and the number of SLM pixels. The propagation dynamics of the *CASE* I Airy beam can now be written as follows using the Fresnel diffraction form of Eq. (2.4):

$$\begin{aligned}\phi_1(x,z) = &\int_{-\infty}^{\infty} \Pi\left(\frac{\lambda f}{2\pi l}k\right)\exp\left(-ax_0^2k^2\right) \\ &\times\exp\left(\frac{i}{3}\left(x_0^3k^3 - 3a^2x_0k - ia^3\right) - i\frac{z}{2k_0}k^2\right)\exp(+ikx)dk,\end{aligned} \tag{2.7}$$

where the value of a is chosen to be 0.1 throughout this chapter. Calculation results of Eq. (2.7) are plotted in Fig. 2.1(a). In this case, the number of side lobes in the initial plane

(z=0 cm) is decreased because the Gaussian distribution of the input beam cannot fully retain the high spatial frequency components. It is known that side lobes of Airy beams are originated form high spatial frequency components. As a result, unlike the ideal case shown in Fig. 2.1(d), the Airy beam is diffracted or spreads out due to insufficient power flows from the side lobes.

Second, under the same conditions, a beam with a uniform intensity distribution of finite extent (or a truncated plane wave as an input beam; *CASE* II) is adopted. In this case, it has

$$\Phi_2(k) = \Pi\left(\frac{\lambda f}{2\pi l}k\right)\exp\left(i\frac{k^3}{3}\right). \tag{2.8}$$

From the property of the Fourier transform, the (inverse) Fourier transform of Eq. (2.8) is a convolution of the sinc function and the Airy function as follows:

$$\phi_2(x, z=0) = \mathrm{sinc}\left(\frac{l}{\lambda f}x\right) * \mathrm{Ai}\left(\frac{x}{x_0}\right), \tag{2.9}$$

where * denotes the convolution. The propagation dynamics of the *CASE* II Airy beam can be expressed as:

$$\phi_2(x, z) = \int_{-\infty}^{\infty} \Pi\left(\frac{\lambda f}{2\pi l}k\right)\exp\left(i\frac{(x_0 k)^3}{3} - i\frac{z}{2k_0}k^2\right)\exp(+ikx)dk, \tag{2.10}$$

and its calculation results are presented in Fig. 2.1(b). In Fig. 2.1(b), more side lobes at the initial plane compared with the *CASE* I are observed. Figure 2.1(b) also shows that the incidence of a truncated plane wave and its Fourier transform after the cubic phase modulation can generate a finite power Airy beam which takes up a bending trajectory with the acceleration toward the $+x$ direction. What is interesting is that this finite Airy beam can preserve its Airy profile much farther than that generated by the Gaussian input beam. This is because more high-frequency components are retained in Eq. (2.8) than in Eq. (2.6). That is, the $\mathrm{sinc}\left(\frac{l}{\lambda f}x\right)$ term resulting in imposing finite power in Eq. (2.9) is keeping more side lobes of Airy beams than exponentially decaying term exp(as).

Lastly, in the *CASE* III, I use a beam with an inverse Gaussian intensity distribution as an input beam. I have

$$\phi_3(x,z) = \int_{-\infty}^{\infty} \Pi\left(\frac{\lambda f}{2\pi l}k\right)\left(1-\exp\left(-ax_0^2k^2\right)\right) \times \exp\left(\frac{i}{3}\left(x_0^3k^3 - 3a^2x_0k - ia^3\right) - i\frac{z}{2k_0}k^2\right)\exp(+ikx)dk. \tag{2.11}$$

In this case, whose results are shown in Fig. 2.1(c), the main lobe is suppressed at the initial plane because the inverse Gaussian distribution can retain only high spatial frequency components. However, as can be found in Fig. 2.1(c), the resultant finite power beam generates the main lobe after some propagation distance and is accelerated along the $+x$ direction. That is, Eq. (2.11) also describes a finite power Airy beam. Actually, this case can be taken as an extreme example proving the self-healing property [4, 5]: side lobes without the main lobe can regenerate the Airy profile during the propagation.

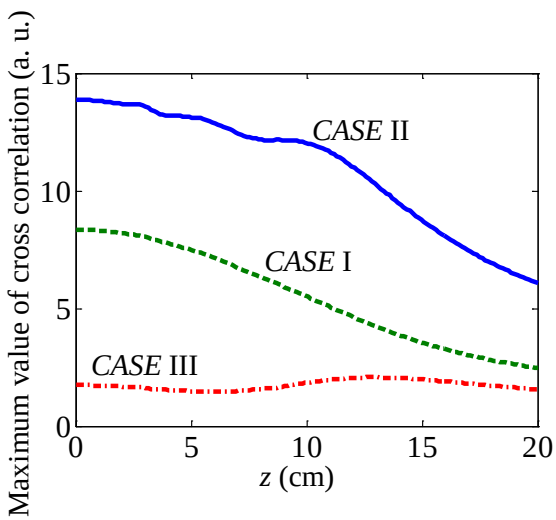

Figure 2.2 Cross-correlations of finite power Airy beams with the ideal Airy beam along the propagation direction: $C_1(z)$.

To compare the propagation characteristics of these three finite power Airy beams, their cross-correlations with the ideal Airy beam are calculated along the propagation

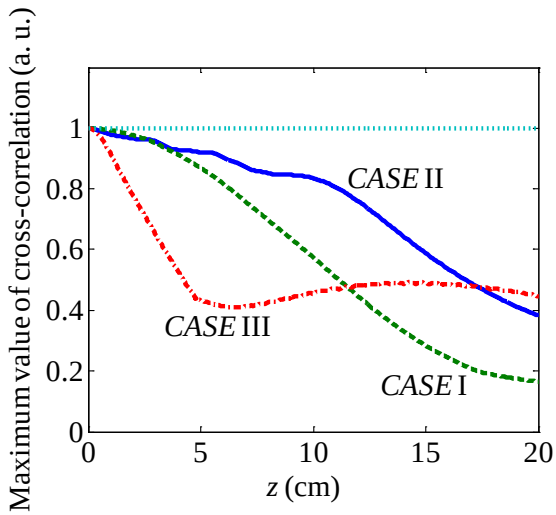

Figure 2.3 Cross-correlation between profiles at the initial plane and at a specific position z calculated in the direction of the propagation (z-direction): $C_2(z)$. A cyan dotted line denotes ideal Airy beams. All values are normalized by the cross-correlation value at the initial plane.

direction z. In Fig. 2.2, the variation of the maximum value of this cross-correlation is plotted, i.e., $C_1(z)$ defined by

$$C_1(z) = \max\left(\int_{-\infty}^{+\infty} \left|\phi_0^*(\tau)\right|^2 \left|\phi_{i=1,2,3}(x+\tau)\right|^2 d\tau \right). \tag{2.12}$$

Green dashed, blue solid and red dash-dotted lines correspond to the *CASE* I, II and III, respectively. Although the cross-correlation values in Fig. 2.2 cannot be normalized due to infinite power of ideal Airy beams, it can be known that the cross-correlation becomes maximum at the initial plane and gradually decreases for the *CASE* I and II. This means that the finite power Airy beams spread out or are diffracted so that they lose their initial Airy shape during propagation. However, it shows that the cross-correlation value of the *CASE* II Airy beam is always higher than that of the *CASE* I at every z. This means that the *CASE* II Airy beam can preserve its original shape much farther than the *CASE* I Airy beam. In the *CASE* III, however, the cross-correlation increases after some propagation

distance. This indicates the recovery process of the Airy profile: the regeneration of the main lobe and its acceleration along the transverse coordinate.

In addition, by comparing the cross-correlations of each beam at a specific position of z with their initial profiles, we can know how far they maintain their initial Airy distributions. The variation of the maximum value of this cross-correlation, i.e., $C_2(z)$ defined by

$$C_2(z) = \max\left(\int_{-\infty}^{+\infty} \left|\phi^*_{i=0,1,2,3}(\tau; z=0)\right|^2 \left|\phi_{i=0,1,2,3}(x+\tau)\right|^2 d\tau \right) \tag{2.13}$$

is plotted in Fig. 2.3. Naturally, the maximum cross-correlation values of ideal Airy beams (cyan dotted line) are constant from z= 0 cm to z=20 cm. For all other cases, they are gradually losing their initial Airy distributions during propagations. Over 2.6 cm, the *CASE* II is more slowly decreased than the *CASE* I. That is, a uniform distribution input case maintains their initial Airy distributions during propagations than those of a Gaussian distribution input case. The *CASE* III shows a nearly flat line from 5 cm. From the results of the *CASE* III in Figs. 2.2 and 2.3, I assume that the self-healing is observed after 5 cm.

Meanwhile, let us consider truncation effects on the non-diffraction property of Airy beams. For example, the more SLM pixels are increased, the more high spatial frequency components are passed. As a result, side lobes of Airy beams are increased and more power is supplied. In case of twice as much pixels, propagation dynamics of finite power Airy beams generated by a Gaussian beam, a uniform beam of finite extent and an inverse Gaussian beam is shown in Figs. 2.4(a), 2.4(b) and 2.4(c), respectively. Although a frequency window is wider, propagation dynamics of the *CASE* I is much the same comparing Figs. 2.1(a) and 2.4(a). However, the *CASE* II shows more similar propagation with ideal Airy beams comparing Figs. 2.1(b), 2,1(d) and 2.4(b). In the *CASE* III in Fig. 2.4(c), the focused-bending beam is more apparent than Fig. 2.1(c). In addition, the self-healing property is improved due to more side lobes. On the contrary, in case of half as much pixels, propagation dynamics of each finite power Airy beams *CASE* is shown in Figs. 2.4(d), 2.4(e) and 2.4(f), respectively. The *CASE* I and *CASE* II

show the similar propagation dynamics and more diffraction takes place in both *CASES*. As a result, a distance with keeping Airy profile is shorter than that of previous *CASES*. Also, the *CASE* III cannot reconstruct the finite power Airy beams due to lack of power from the side lobes. Therefore, to generate the finite power Airy beams under limiting experimental conditions, using a uniform beam of finite extent is suitable not only to closely generate the ideal Airy beams but also to preserve its Airy profile during propagations.

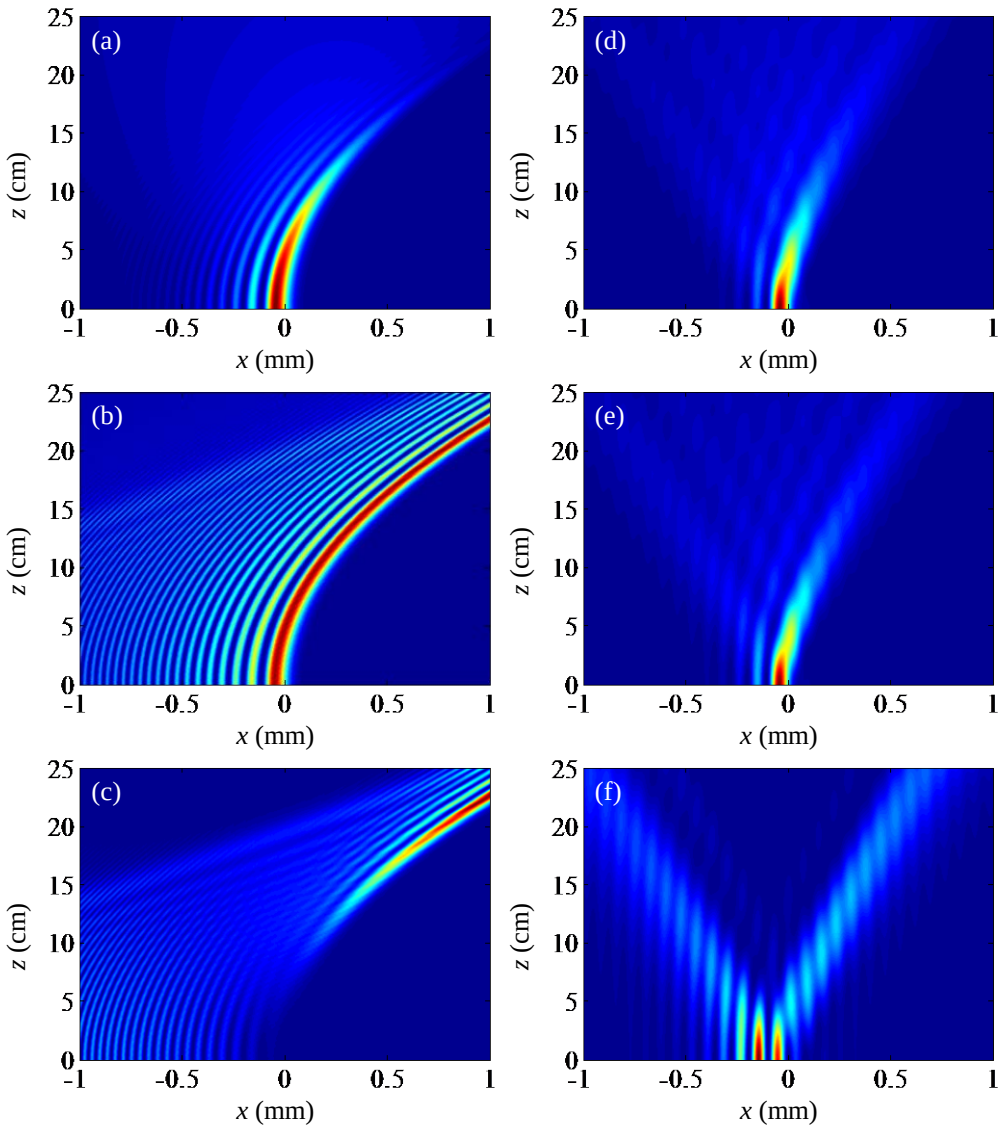

Figure 2.4 Propagation dynamics of finite power Airy beams in case of twice as much pixels generated by (a) a Gaussian beam, (b) a uniform beam of finite extent and (c) an inverse Gaussian beam. Propagation dynamics of finite power Airy beams in case of a half as much pixels generated by (d) a Gaussian beam, (e) a uniform beam of finite extent and (f) an inverse Gaussian beam.

2.1.3. (2+1)D finite power Airy beams

Now, let us consider (2+1)D finite power Airy beams. In this case, it is assumed that the wavelength of an incident beam λ is 633 nm, x_0 is 50 μm, the focal length of the lens f is 50 cm and the SLM has 1080 × 1080 pixels with an 8 μm pixel pitch. Equations (2.7), (2.10) and (2.11) are modified as

$$\begin{aligned}\phi_1(x,y,z) = &\prod_{\chi=x,y}\int_{-\infty}^{\infty}\Pi\left(\frac{\lambda f}{2\pi l_\chi}k_\chi\right)\exp\left(-a\chi_0^2k_\chi^2\right)\\ &\times\exp\left(\frac{i}{3}\left(\chi_0^3k_\chi^3-3a^2\chi_0k_\chi-ia^3\right)-i\frac{z}{2k_0}k_\chi^2\right)\exp(+ik_\chi\chi)dk_\chi,\end{aligned} \tag{2.14}$$

$$\phi_2(x,y,z) = \prod_{\chi=x,y}\int_{-\infty}^{\infty}\Pi\left(\frac{\lambda f}{2\pi l_\chi}k_\chi\right)\exp\left(i\frac{\left(\chi_0k_\chi\right)^3}{3}-i\frac{z}{2k_0}k_\chi^2\right)\exp(+ik_\chi\chi)dk_\chi, \tag{2.15}$$

and

$$\begin{aligned}\phi_3(x,y,z) = &\prod_{\chi=x,y}\int_{-\infty}^{\infty}\Pi\left(\frac{\lambda f}{2\pi l_\chi}k_\chi\right)\left(1-\exp\left(-a\chi_0^2k_\chi^2\right)\right)\\ &\times\exp\left(\frac{i}{3}\left(\chi_0^3k_\chi^3-3a^2\chi_0k_\chi-ia^3\right)-i\frac{z}{2k_0}k_\chi^2\right)\exp(+ik_\chi\chi)dk_\chi,\end{aligned} \tag{2.16}$$

which correspond to the *CASE* I, II and III Airy beams, respectively, where l_x and l_y are the horizontal and vertical lengths of the SLM and y_0 is an arbitrary scaling factor along the y coordinate.

Calculated 2D intensity distributions of (2+1)D finite power Airy beams are shown in Figs. 2.5(a) and 2.5(b) (ϕ_1; *CASE* I), Figs. 2.5(c) and 2.5(d) (ϕ_2; *CASE* II) and Figs. 2.5(e) and 2.5(f) (ϕ_3; *CASE* III). Figures 2.5(a), 2.5(c), 2.5(e) and 2.5(b), 2.5(d), 2.5(f) are the results at z=0 cm and z=15 cm, respectively. Comparing Figs. 2.5(a), 2.5(c) and 2.5(e), more side lobes in Fig. 2.5(c) than in Fig. 2.5(a), while the main lobe disappears in Fig. 2.5(e), can be found. After some propagation (z=15 cm), the finite power Airy beam generated by a Gaussian beam (*CASE* I) does not preserve its initial Airy profile anymore. On the other hand, the finite power Airy beam generated by a truncated plane

wave (or a uniform beam of finite extent; *CASE* II) maintains its initial profile although the beam is broadened due to the diffraction. Therefore, the uniform beam of the *CASE* II is more advantageous than the Gaussian beam of the *CASE* I. In the case of the inverse Gaussian beam (*CASE* III), although the main lobe is missing at the initial plane (Fig. 2.5(e)), side lobes recover the main lobe after some propagations as can be found in Fig. 2.5(f).

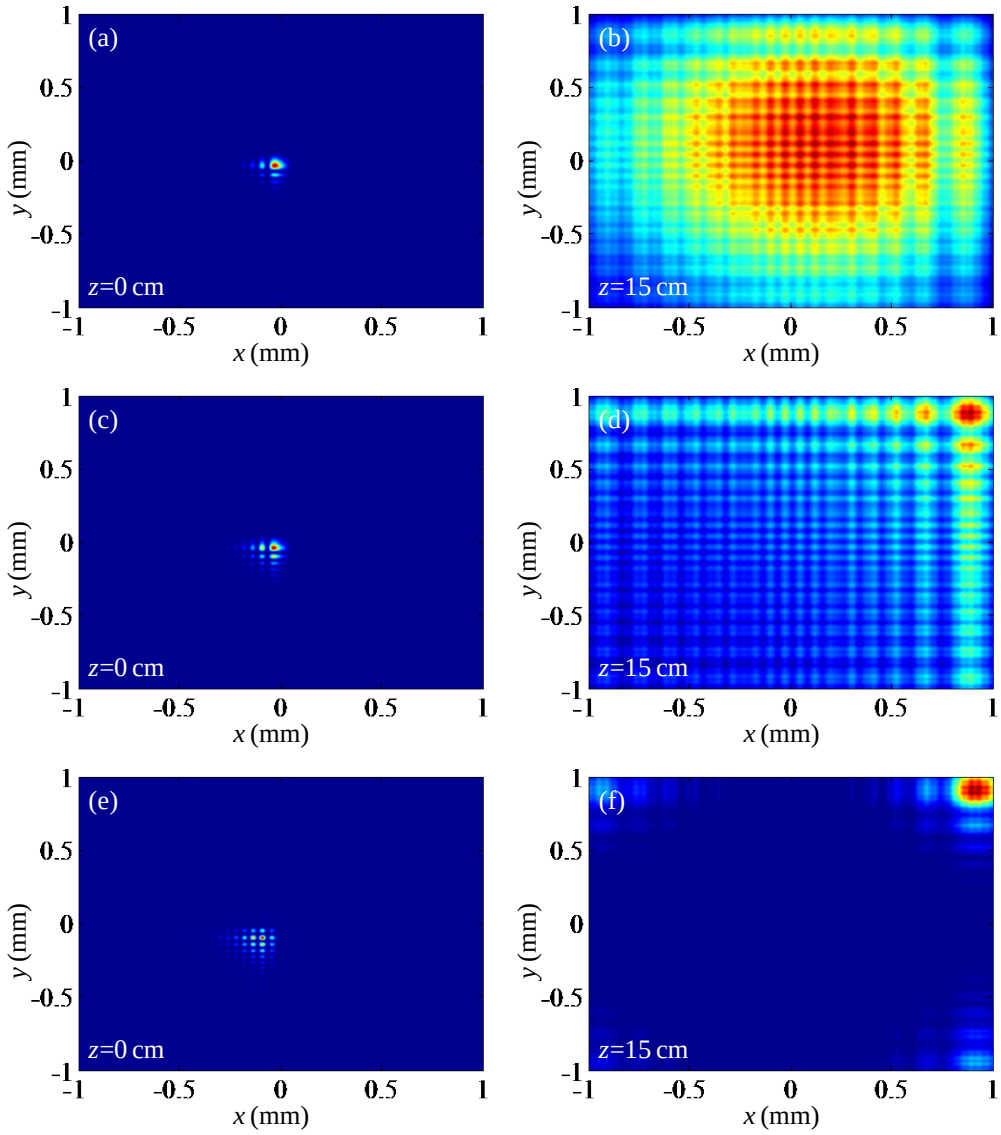

Figure 2.5 Intensity distributions of (2+1)D finite power Airy beams. *CASE* I: (a) at z=0 cm and (b) z=15 cm. *CASE* II: (c) at z=0 cm and (d) z=15 cm. *CASE* III: (e) at z=0 cm and (f) z=15 cm.

2.2. Experiments of finite power Airy beams

The generation of the finite power Airy beams to three *CASES* is experimentally demonstrated. The conventional method to generate finite power Airy beams used one SLM wrapping phases to an incident Gaussian beam. The two SLMs function not only as phase wrapping device to incident beams but also as modulator of initial fields such as a conventional Gaussian distribution (*CASE* I), a uniform distribution of finite extent (*CASE* II) and an inverse Gaussian distribution (*CASE* III). This work will promise to know roles of initial field distributions.

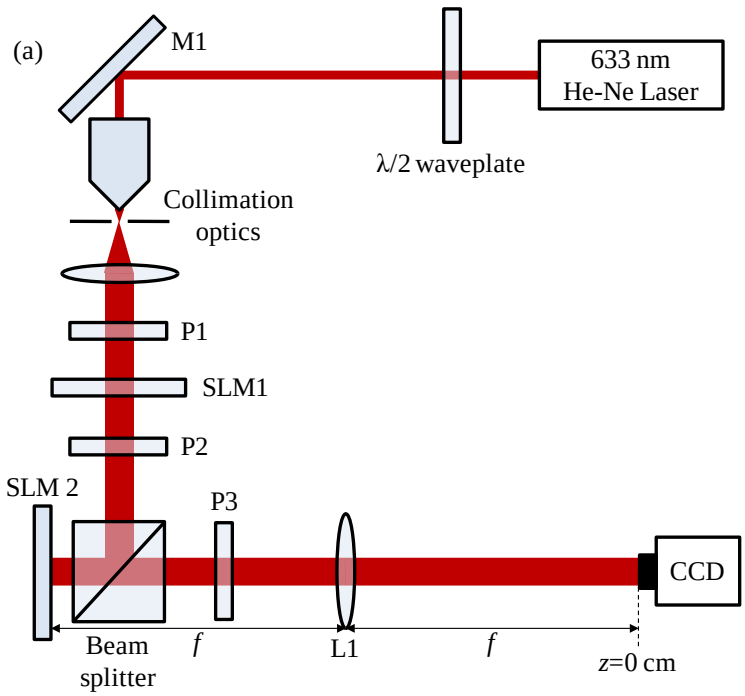

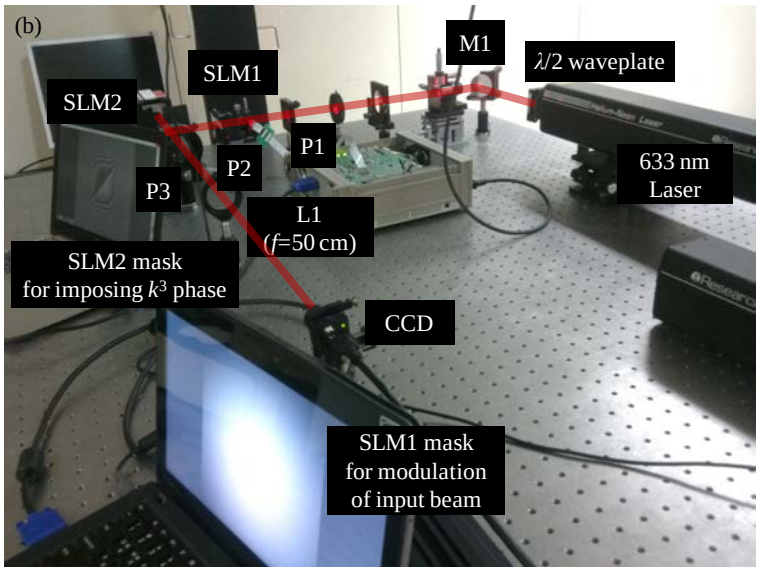

Figure 2.6 (a) Schematic diagram. M1 is a mirror, P1, P2 and P3 are polarizers and L1 is a lens with f=50 cm. (b) Experimental setup for the generation of finite power Airy beams.

2.2.1. Experimental setup

Figures 2.6(a) and 2.6(b) show the schematic diagram and the experimental setup for the generation of finite power Airy beams, respectively. A laser beam with a 633 nm wavelength is expanded to form a collimated plane wave. To change this input wave into the Gaussian, inverse Gaussian or uniform beam of finite extent, the SLM1 (Mitsubishi Electric *XL9U* LCD projector with 1024 × 768 pixels of 11.9 μm pixel pitch) is placed between two orthogonal linear polarizers (P1 and P2) [53]. These polarizers allow the SLM1 to perform intensity modulations. Corresponding phase masks are shown in Figs. 2.7(a), 2.6(b) and 2.6(c), respectively. *x*- and *y*-resolutions of the SLM1 are not a square, only 768 × 768 pixels are used to modulate input beams. As a result, the rest of 768 × 768 pixels are filled with white. After passing through the SLM1, the beams have a Gaussian distribution (*CASE* I, Fig 2.7(d)), a uniform distribution of finite extent (*CASE* II, Fig. 2.7(e)) or an inverse Gaussian distribution (*CASE* III, Fig 2.7(f)).

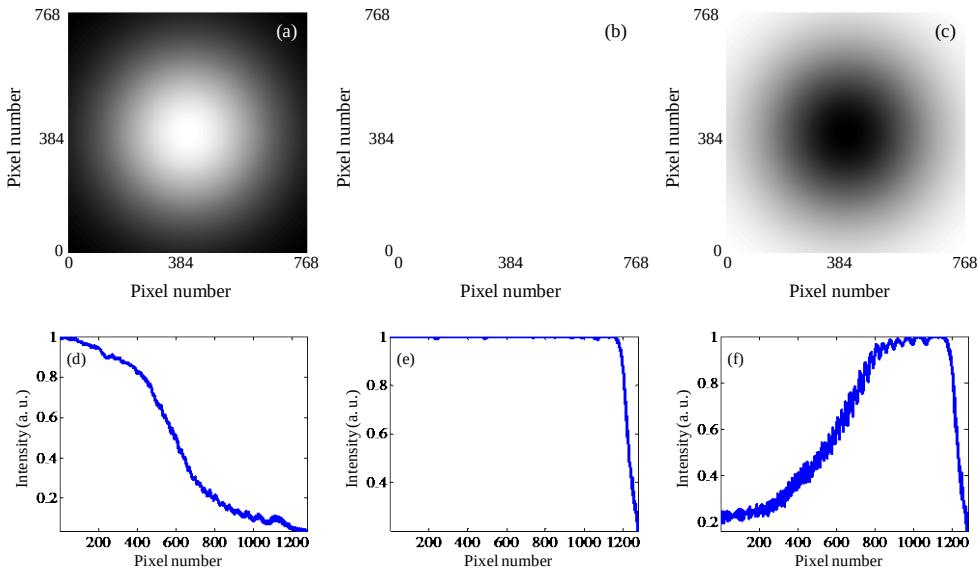

Figure 2.7 Phase mask for modulating initial beams: (a) Gaussian distribution, (b) uniform distribution of finite extent and (c) inverse Gaussian distribution. Measured intensity distribution by the CCD after passing through the SLM1: (d) Gaussian distribution, (e) uniform distribution of finite extent and (f) inverse Gaussian distribution.

By passing these beams through the optical Fourier transform (2-*f*) system, finite power Airy beams at the initial plane (z=0 cm) can be obtained. The optical Fourier transform system consists of a lens (L1; f=50 cm) and a phase-only SLM2 (Holoeye *Pluto* with 1920 × 1080 pixels of 8 μm pixel pitch) which is placed in front of the lens and imposes cubic (k^3) phase. The same computer-generated cubic phase mask (Fig. 2.8) is used to all *CASES* because the higher-order phase terms can be ignored due to the relatively small constant a. Similarly, x- and y-resolutions of SLM2 are not a square, only 1080 × 1080 pixels are used to modulate beams. As a result, the rest of 1080 × 1080 pixels are filled with black. To obtain clear Airy beam images, a blazed grating is overwrapped in the cubic phase mask [54]. As a result, when an initial beam with a normal incidence is reflected by the SLM2, the 1st order beam is propagating along an

optical axis and the 0^{th} order beam is propagating with an oblique angle. Another polarizer P3 is used to attenuate the output beam so that a twin image can be eliminated.

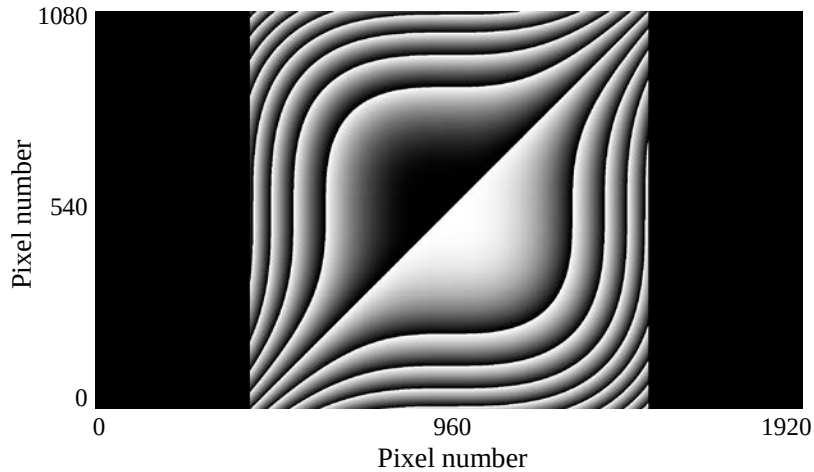

Figure 2.8 Phase mask for launching (2+1)D Airy beams: x_0=50 μm, y_0=50 μm and a=0.1. The cubic phase is wrapped without the higher-order phase terms.

2.2.2. Experimental results

To obtain exact experimental results, perfect alignment must be preceded before observing acceleration of Airy beams. Especially, if the beam reflected from the SLM2 does not propagate along the optical axis, it is difficult to observe acceleration of Airy beams. A target image mask which is provided by Holoeye to adjust alignment between the SLM2 and the charge-coupled device (CCD) is used. At first, the vivid target image z=0 cm (Fourier plane) shown in Fig. 2.9(a) is captured. Then, the cross pattern of the target image is clearly seen without the 0^{th} order diffraction due to a blazed grating with a proper period. Next, moving the CCD from z=0 cm to z=15 cm, the target image, which is shown in Fig. 2.9(b) is captured again. It shows the blurring cross pattern but the center of the image maintains the initial position, qualitatively. Therefore, throughout this dissertation, the errors from misalignment were neglected.

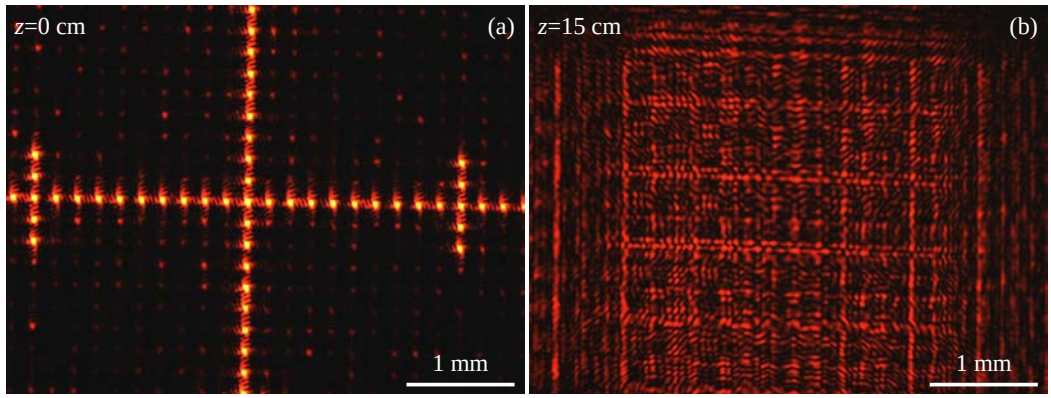

Figure 2.9 The cross patterns of the target image at (a) z=0 cm and (b) z=15 cm.

The images of the finite power Airy beams were captured by the CCD at z=0 cm and z=15 cm and shown in Figs. 2.10(a) - 2.10(f). All images are obtained under the same conditions that no adjustments in intensities were made. From these results, it can be concluded that the *CASE* II Airy beam [Figs. 2.10(c) and 2.10(d)] retains the Airy profile much longer than the *CASE* I Airy beam [Figs. 2.10(a) and 2.10(b)]. Meanwhile, the *CASE* III Airy beam recovers the main lobe at z=15 cm as shown in Figs. 2.10(e) and 2.10(f). These experimental results coincide well with the calculation results shown in Figs. 2.5(a) - 2.5(f).

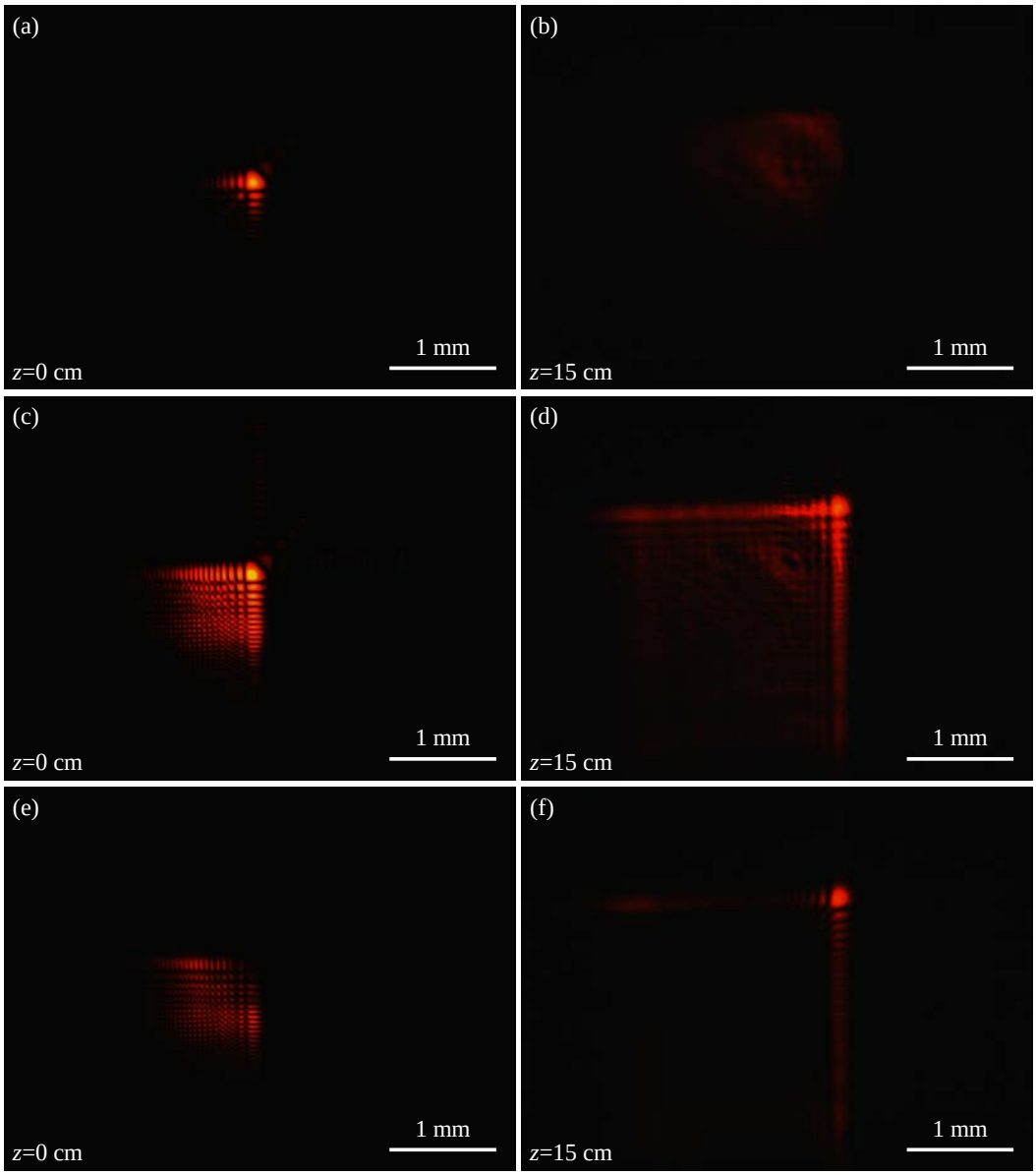

Figure 2.10 Captured CCD images of finite power Airy beams. *CASE* I: (a) at z=0 cm and (b) z=15 cm. *CASE* II: (c) at z=0 cm and (d) z=15 cm. *CASE* III: (e) at z=0 cm and (f) z=15 cm.

Chapter 3.

Generation of Airy beams by holographic method

In this chapter, the novel Airy beam generation method based on holography is present. The holographic finite power Airy beams can be obtained by recording the interference patterns between the Airy beams and the reference beam on a photopolymer and reconstruction under illuminations of the reference beam. This method has several advantages as the following. After they are recorded in the photopolymer, a bulky optical setup such as the SLM and lenses is unnecessary to generate Airy beams. That is, simple generation illuminating the reference beam is possible. Also, by the use of the phase-conjugated reference beam to reconstruct the recorded Airy beams, the Airy beams with the reversed propagation direction keeping its original amplitudes and phases and more bent symmetric Airy beam can be generated. Since this method is possible to realize angle multiplexing of the two Airy beams accelerating in opposite directions determined by the angle of the reference beams, it is expected to utilize to be used as a practical approach in the applications such as particle manipulation and optical signal processing.

3.1. Holographic generation of Airy beams

So far it is impossible to implement the optical Airy beams because ideal Airy beams impose infinite power. However, in 2007, Siviloglou and Christodoulides, announced that finite energy Airy beams can be achieved by tailoring side lobes with an aperture function and they have similar propagating characteristics by comparison with the ideal

Airy beams [2]. Based on this report, the first optical observation of the Airy beams was realized by the optical Fourier transform system which is adding the cubic phase to a broad Gaussian beam using the spatial light modulator (SLM) [3]. On the same principle, observations of Airy beams in wide area such as nonlinear generation [29-31], curved plasma channel generation [32] and electron beam generation [33] were reported.

The way to generate Airy beams which directly assigns initial launching conditions was suggested. By matching initial intensity and phase distributions of Airy beams and that of surface plasmon polaritons (SPPs) after passing through the metal slits or gratings, (1+1)D Airy beams can be launched: Airy plasmon which has longer propagation length than other surface waves [21-27]. Also, through the grating on the metal surface, generated Airy beams in free space can be coupled to Airy plasmons which have dynamically controlled trajectories by controlling the position of the objective lens or the phase mask on the SLM [25].

In this chapter, a novel Airy beam generation technique based on holography is presented [49]. At first, using the optical Fourier transform system, Airy beam can be generated in free space. Second, the interference patterns between the generated Airy beams (signal beam) and reference beam are recorded on a photopolymer. Finally, when the photopolymer is exposed by the reference beam with blocking the signal beam, recorded Airy beams are reconstructed from the plane of the photopolymer. It is shown that generated Airy beams maintain non-diffracted nature with a bending trajectory after holographic recording and reconstruction procedures.

In case of the (2+1)D finite power Airy beams at the origin (z=0 cm), Eq. (2.5) can be expanded to

$$\phi(x, y, z = 0\,\mathrm{cm}) = \mathrm{Ai}\left(\frac{x}{x_0}\right)\exp\left(a\frac{x}{x_0}\right)\mathrm{Ai}\left(\frac{y}{y_0}\right)\exp\left(a\frac{y}{y_0}\right), \tag{3.1}$$

where x_0 and y_0 are arbitrary scaling factors of x- and y-coordinates, respectively. Throughout this chapter, parameters for the finite power Airy beams, x_0, y_0 and a are set to 50 μm, 50 μm and 0.1, respectively and operating wavelength is 633 nm. The intensity distributions of the (2+1)D finite power Airy beams at z=0 cm, z=5 cm and z=15 cm in

Figs. 3.1(a), 3.1(b) and 3.1(c), respectively, are plotted.

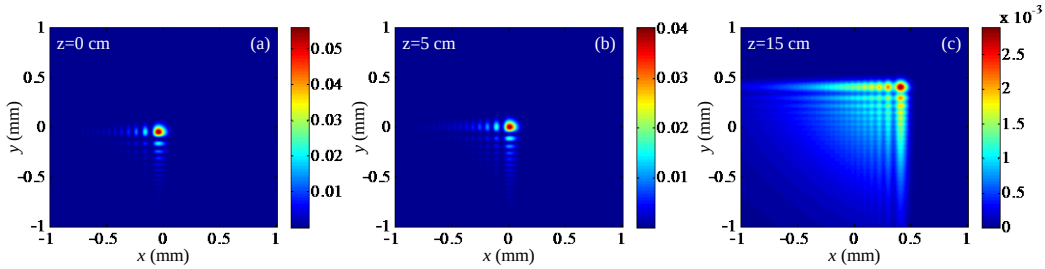

Figure 3.1 Intensity distributions of the (2+1)D finite power Airy beams (a) at z=0 cm, (b) z=5 cm and (c) z=15 cm.

3.1.1. Holographic recording of Airy beams

Holography is a technique which can record and reconstruct both the amplitude and the phase of the optical wave [55]. It consists of two steps: recording and reconstruction. The mathematical representation for the (2+1)D finite power Airy beam ϕ is given by

$$\begin{aligned}\phi(x,y,z) &= \prod_{\chi=x,y} \mathrm{Ai}\left(\frac{\chi}{\chi_0} - \frac{z^2}{4k^2\chi_0^4} + ia\frac{z}{k\chi_0^2}\right) \\ &\times \exp\left(a\frac{\chi}{\chi_0} - a\frac{\chi^2}{2k^2\chi_0^4} + ia^2\frac{z}{2k\chi_0^2} + i\frac{\chi z}{2k\chi_0^3} - i\frac{z^3}{12k^3\chi_0^6}\right),\end{aligned} \tag{3.2}$$

where k=2$\pi n/\lambda_0$. The optical intensity I of the (2+1)D finite power Airy beams is obtained by taking the square modulus of Eq. (3.2):

$$\begin{aligned}I(x,y,z) &= \mathrm{Ai}^2\left(\frac{x}{x_0} - \frac{z^2}{4k^2x_0^4} + ia\frac{z}{kx_0^2}\right)\exp\left(2a\left(\frac{x}{x_0} - \frac{x^2}{2k^2x_0^4}\right)\right) \\ &\times \mathrm{Ai}^2\left(\frac{y}{y_0} - \frac{z^2}{4k^2y_0^4} + ia\frac{z}{ky_0^2}\right)\exp\left(2a\left(\frac{y}{y_0} - \frac{y^2}{2k^2y_0^4}\right)\right).\end{aligned} \tag{3.3}$$

Here, the transmittance t is proportional to the intensity distributions. That is, the transmittance is defined by

$$t(x,y) = hI(x,y), \tag{3.4}$$

where h is a constant. Since the photopolymer is placed at z=0 cm, the transmittance t_o of

the (2+1)D finite power Airy beams is expressed by

$$t_o(x,y) = \mathrm{Ai}^2\left(\frac{x}{x_0}\right)\exp\left(2a\frac{x}{x_0}\right)\mathrm{Ai}^2\left(\frac{y}{y_0}\right)\exp\left(2a\frac{y}{y_0}\right). \tag{3.5}$$

A uniform plane wave as a reference beam U_r with an incident angle θ has a complex amplitude, which is given by

$$U_r(x,y) = \exp\left(-ikx\sin\theta\right)\exp\left(-jk\left(x\sin\theta + z\cos\theta\right)\right). \tag{3.6}$$

In addition, interference patterns t between an object beam (ϕ; Eq. (3.2)) and a reference beam (U_r; Eq. (3.6)) are recorded on the photopolymer:

$$\begin{aligned} t &\propto \left(\phi + U_r\right)^2 = \left|\phi\right|^2 + \left|U_r\right|^2 + \phi^* U_r + \phi U_r^* \\ &= t_o + I_r + \phi U_r^* + \phi^* U_r \\ &= t_o + I_r + 2\sqrt{t_o I_r}\cos\left[\arg(U_r) - \arg(\phi)\right], \end{aligned} \tag{3.7}$$

where I_r is the intensity of the reference beam at z= 0 cm.

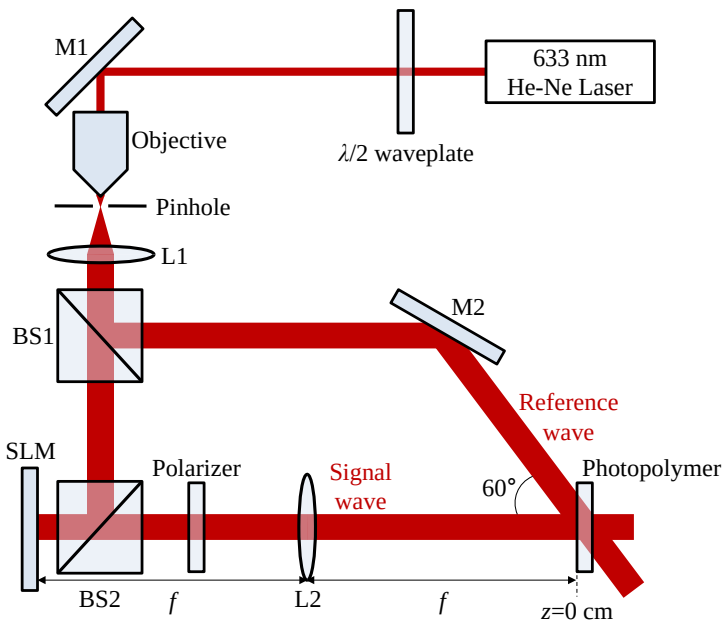

Figure 3.2 Schematic diagrams of recording for generating the (2+1)D holographic Airy beams. (M: mirror, L: lens, BS: beam splitter)

Figure 3.2 is a schematic diagram of recording procedures. After passing through the beam splitter 1 (BS1), a plane wave from the He-Ne laser with 633 nm wavelength is divided into the signal arm and the reference arm. In the signal arm, a 2-*f* system consists of the SLM (Holoeye Pluto, reflection type, 1920 × 1080 pixels, 8 μm pixel pitch) which imposes the computer-generated cubic phase mask and the lens 2 (L2) with the focal length *f* (=50 cm). Two phase masks are made for launching the (2+1)D finite power Airy beams bent in different directions which are +*x* and +*y* directions with the phase mask 1 (x_0=50 μm and y_0=50 μm) and -*x* and -*y* directions with the phase mask 2 (x_0=-50 μm and y_0=-50 μm) as shown in Figs. 3.3(a) and 3.3(b), respectively. The L2 with a distance *f* apart from the SLM (object plane) is placed to perform the optical Fourier transform. A $\lambda/2$ wave plate and a linear polarizer are used to adjust states of the polarization and eliminate twin images, respectively.

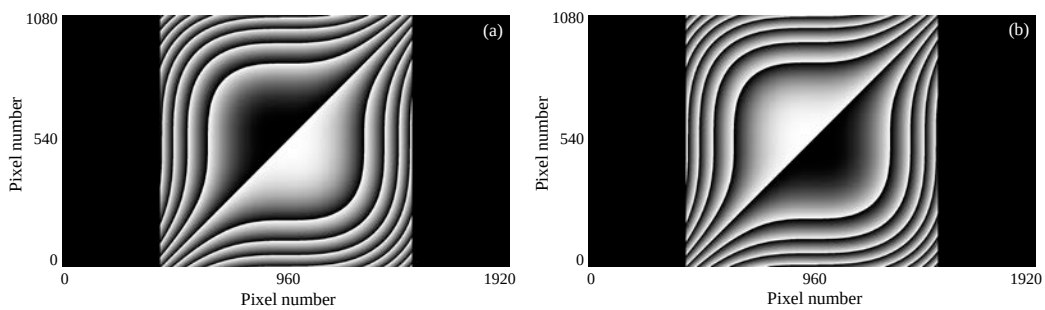

Figure 3.3 Phase mask for launching (2+1)D Airy beams: (a) x_0=50 μm, y_0=50 μm and a=0.1. (b) (a) x_0=-50 μm, y_0=-50 μm and a=0.1. The cubic phase is wrapped without the higher-order phase terms.

After the signal beam is reflected in the SLM and travels *f* after passing through the L2, the finite power Airy beams at the Fourier plane (z=0 cm) can be obtained, successively. Before the recording procedure, the charge-coupled device (CCD) is located to confirm the optical reconstruction of the finite Airy beams. The resultant captured images of the (2+1)D finite power Airy beams at z=0 cm, z=5 cm and z=15 cm are shown in Figs. 3.4(a), 3.4(b) and 3.4(c), respectively. After that, interference patterns between the signal beam (Airy beam) and the reference beam (plane wave) are recorded on the photopolymer. In this procedure, the reference beam has an incident angle of 60°

with 32 mJ/cm^2 energy density and exposure time is 40 seconds. Throughout this chapter, incident angles from 30° to 70° have similar diffraction efficiency of near 50 %. The incident angle of the reference beam 60° is determined by achieving the maximum diffraction efficiency of 51 %. A holographic film on a slide glass of 1.518 refractive index is used as a holographic photopolymer because it is easy to handle and has the simple post exposure processing. It consists of two layers which are a photopolymer layer with 14 ~ 18 μm thickness and an optically clear plastic substrate with 175 μm thickness. The refractive index of the used photopolymer is 1.485 before recording at 633 nm wavelength of incident light and has index change as much as 0.03. The substrate index is 1.57 at 589 nm wavelength of incident light. For curing, the recorded sample is exposed by the UV-lamp with 110 mW/cm^2 power density during 3 minutes and the distance between the UV-lamp and the sample is 30 cm.

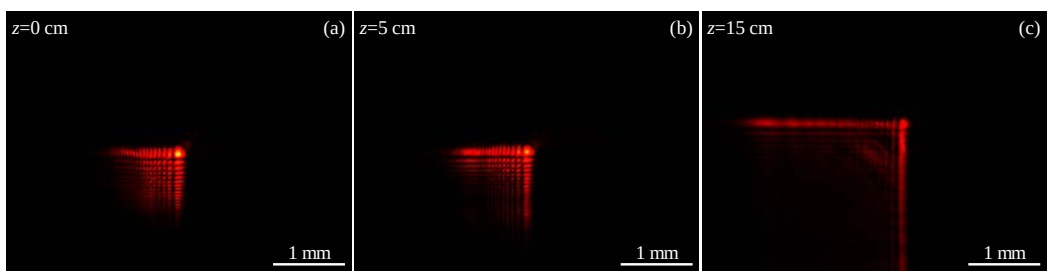

Figure 3.4 Captured CCD images of the (2+1)D finite power Airy beams (a) at z=0 cm, (b) z=5 cm and (c) z=15 cm. Camera settings are the same.

3.1.2. Holographic reconstruction of Airy beams

To reconstruct the Airy beams (object beam) from the recorded hologram, the reference wave U_r with the same incident angle θ illuminates the recorded sample. The resultant reconstructed wave ϕ_r is expressed as below:

$$\phi_r = tU_r \propto t_o U_r + I_r U_r + \phi I_r + \phi^* |U_r|^2 . \tag{3.8}$$

In Eq. (3.8), the physical meaning of the third term ϕI_r is the (2+1)D finite power Airy beams multiplied by the reference beam intensity I_r. That is, this term represents Airy beams which can be reconstructed by the holographic method.

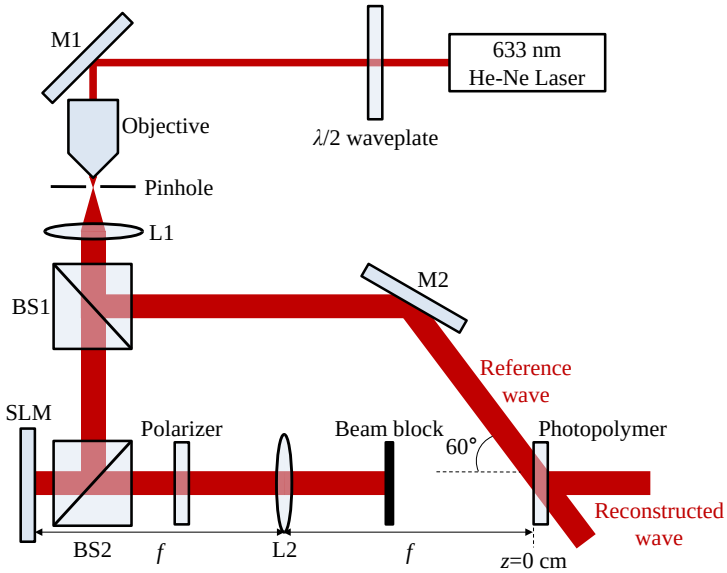

Figure 3.5 Schematic diagrams of reconstruction for generating the (2+1)D holographic Airy beams. (M: mirror, L: lens, BS: beam splitter)

The schematic diagram of the reconstruction procedure is shown in Fig. 3.5. While the signal arm is blocked, the reference beam illuminates the photopolymer. As a result, the (2+1)D finite power Airy beams are generated from the photopolymer without the SLM and the Fourier lens. The intensity distributions of the reconstructed beam are captured at z=5 cm and z=15 cm as shown in Figs. 3.6(a) and 3.6(b), respectively. Since the CCD camera cannot approach in front of the photopolymer surface, the intensity distribution of the reconstructed beam at z=0 cm cannot be presented. These results show slight differences in comparison with simulation results and CCD images generated by the SLM. This is resulted from scattering in non-uniform grating originated from the non-uniform shrinkage according to thickness of the photopolymer in curing process [56] and at bubbles between the film and the slide glass. However, reconstructed Airy beams show similar intensity distributions at z=5 cm which are Figs. 3.1(b), 3.4(b) and 3.6(a). In like manner, after propagating 15 cm, they still coincide well as shown in Figs. 3.1(c), 3.4(c) and 3.6(b). Interestingly, it is known that the reconstructed Airy beams do not lose the characteristics of the Airy beams such as acceleration and non-diffraction during

holographic recording and reconstruction procedures.

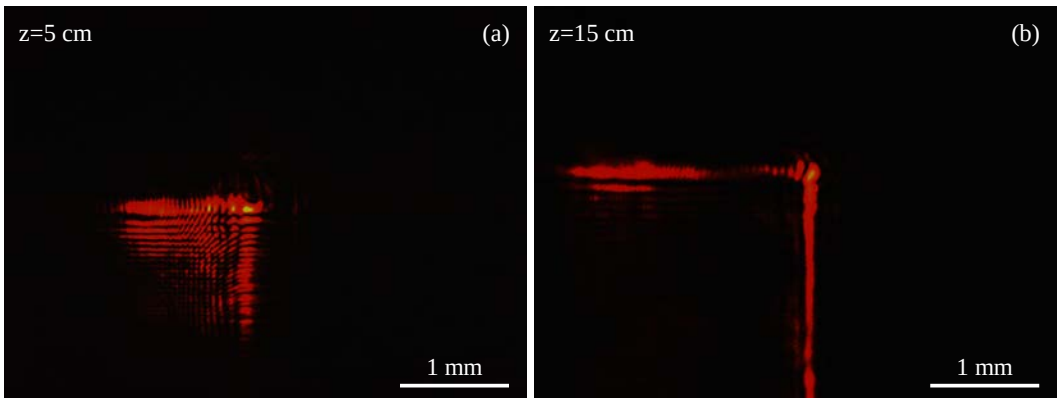

Figure 3.6 Captured CCD images of the reconstructed Airy beams (a) at *z*=5 cm and (b) *z*=15 cm.

3.1.3. Self-healing of Airy beams

In the reconstruction procedure of holography, if the incident reference beam does not fully cover the entire recorded region of hologram, loss of original information is inevitable because angular frequency components of original information are distributed in the entire region. In case of Airy beams, however, it can be inferred that recorded Airy beams can be perfectly reconstructed during propagation under the same conditions. This is originated from the unique self-healing feature of Airy beams. To confirm this property in holography, a part of the reference beam is partially blocked by an opaque obstacle placed between the M2 and the photopolymer instead of shifting incident *x*- and *y*-positions of the reference beam to achieve partial illumination to the recorded region. Especially, by shifting the positions of the obstacle, recorded Airy beams with the suppressed main lobe can be obtained at *z*=5 cm as shown in Fig. 3.7(a). After propagating 10 cm and 15 cm, reconstructed Airy beams recover their original distribution shown in Figs. 3.7(b) and 3.7(c). It is known that the perfect reconstruction of original information is possible despite imperfect incidence of the reference beam. That is, robust generation is possible. Moreover, after Airy beams are reconstructed, they show the self-healing property. When the obstacle blocks the Airy beams between the

photopolymer and the z=5 cm plane, no main lobe can be seen in Fig. 3.7(d). After propagating 10 cm and 15 cm, reconstruction of the veiled region takes place as shown in Figs. 3.7(e) and 3.7(f), respectively.

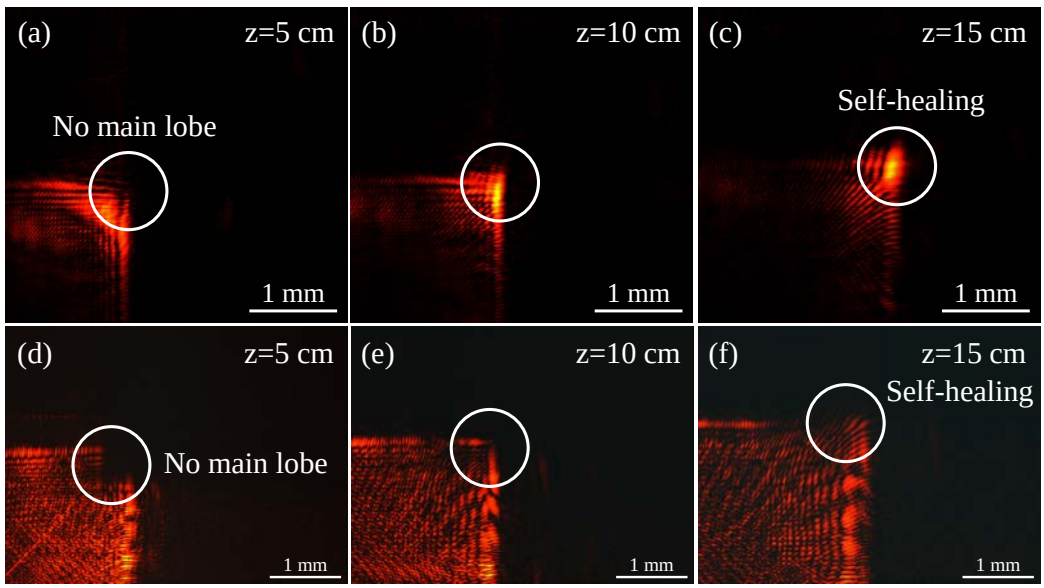

Figure 3.7 Self-healing property for partial illumination (a) at z=5 cm, (b) z=10 cm and (c) at z=15 cm. Self-healing property of reconstructed Airy beams (d) at z=5 cm, (e) z=10 cm and (f) at z=15 cm.

3.1.4. Ballistic trajectory of conjugated Airy beams

In Eq. (2.4), the exponentially decaying factor a imposes finite power to Airy beams. Let us suppose that a is a complex number a_1+$a_2 i$, where a_2 determines the initial launch angle of Airy beams [57]. In this case, the (1+1)D finite power Airy beam ϕ is expressed as

$$\phi(s, \xi = 0) = \mathrm{Ai}(s)\exp(a_1 s)\exp(i a_2 s). \tag{3.9}$$

By solving Eq. (2.1) with the initial condition Eq. (3.9), the (1+1)D finite power Airy beam solution ϕ can be obtained as follows [3]:

$$\phi(s,\xi)=\mathrm{Ai}\left(s-\left(\frac{\xi}{2}\right)^2+ia\xi\right)\exp\left(as-\frac{a\xi^2}{2}+i\left(-\frac{\xi^3}{12}+\frac{a^2\xi}{2}+\frac{s\xi}{2}\right)\right). \tag{3.10}$$

Here, Eq. (3.10) can be rewritten using $a=a_1+a_2i$:

$$\begin{aligned}\phi(s,\xi)=&\mathrm{Ai}\left(s-\left(\frac{\xi}{2}\right)^2-a_2\xi+ia_1\xi\right)\exp\left(a_1s-\frac{a_1\xi^2}{2}-a_1a_2\xi\right)\\ &\times\exp\left(i\left(-\frac{\xi^3}{12}+\left(a_1^2-a_2^2+s\right)\frac{\xi}{2}+a_2s-\frac{a_2\xi^2}{2}\right)\right).\end{aligned} \tag{3.11}$$

Here, different launch angles are considered as shown in Figs. 3.8 which shows the propagation dynamics of the (1+1)D Airy beams in Eq. (3.11) with a=0.1, 0.1+1i and 0.1-1i as a function of z from -25 cm to 25 cm. In case of a_1=0.1 and a_2=0, the ballistic trajectory of Airy beams draws a symmetrically parabolic curve to the z=0 cm axis shown in Fig. 3.8(a). In addition, when a_1=0.1 and a_2=1i, the trajectory has the positive launch angle as shown in Fig. 3.8(b). That is, it shows more bending in z>0 cm and less bending in z<0 cm motions than that of the case with a_1=0.1 and a_2=0. On the contrary to this, when a_1=0.1 and a_2=-1i, the trajectory has the negative launch angle as shown in Fig. 3.8(c). Therefore, it is revealed that the specific position of deflection can be determined by the launch angle parameter a_2.

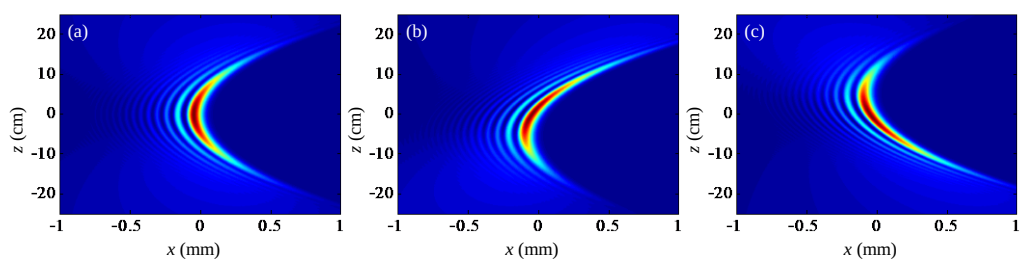

Figure 3.8 Propagation dynamics of the finite power Airy beams when values of a are (a) 0.1, (b) 0.1+1i and (c) 0.1-1i, respectively.

In case of the (2+1)D finite power Airy beam in the initial plane (z=0 cm), Eq. (3.9) can be expanded as following:

$$\phi(x, y, z = 0\ \text{cm}) = \text{Ai}\left(\frac{x}{x_0}\right)\exp\left(a_1\frac{x}{x_0}\right)\exp\left(ia_2\frac{x}{x_0}\right) \times \text{Ai}\left(\frac{y}{y_0}\right)\exp\left(a_1\frac{y}{y_0}\right)\exp\left(ia_2\frac{y}{y_0}\right). \quad (3.12)$$

In like manner, three different cases a of the (2+1)D finite power Airy beams, which are 0.1, 0.1+1i and 0.1-1i, are investigated. When a=0.1 without the complex term, intensity distributions of the (2+1)D finite power Airy beams at z=0 cm, z=15 cm and z=-15 cm are presented in Figs. 3.9(a), 3.9(b) and 3.9(c), respectively. For the same propagation distances of 15 cm and -15 cm in the z-direction, Airy beams have the same intensity distributions as depicted in Figs. 3.9(b) and 3.9(c), respectively. The maximum intensity points of the main lobe are moved from (-0.45 μm, -0.45 μm) to (407 μm, 407 μm) during 15 cm propagation. In case of the positive initial launch angle with a=0.1+1i, intensity distributions at z=0 cm, z=15 cm and z=-15 cm are shown in Figs. 3.9(d), 3.9(e) and 3.9(f), respectively. In this case, propagations in the +z-direction and the -z-direction have different deflection extents. While Airy beams are propagating 0 cm to 15 cm in the z-direction, the maximum intensity points are moved from (-0.45 μm, -0.45 μm) to (709 μm, 709 μm). In addition, while Airy beams are propagating -15 cm to 0 cm in the z-direction, the maximum intensity points are moved from (0.95 μm, 0.95 μm) to (-0.45 μm, -0.45 μm). Finally, in case of the negative initial launch angle with a=0.1-1i, intensity distributions at z=0 cm, z=15 cm and z=-15 cm are depicted in Figs. 3.9(g), 3.9(h) and 3.9(i), respectively. Here, intensity distributions at z=15 cm and z=-15 cm are the same as that of z=-15 cm and z=15 cm with the a=0.1+1i case, respectively. That is, Airy beams are more deflected in z<0 cm and less deflected in z>0 cm. Through all cases, the same intensity distributions are seen in Figs. 3.9(a), 3.9(d) and 3.9(g).

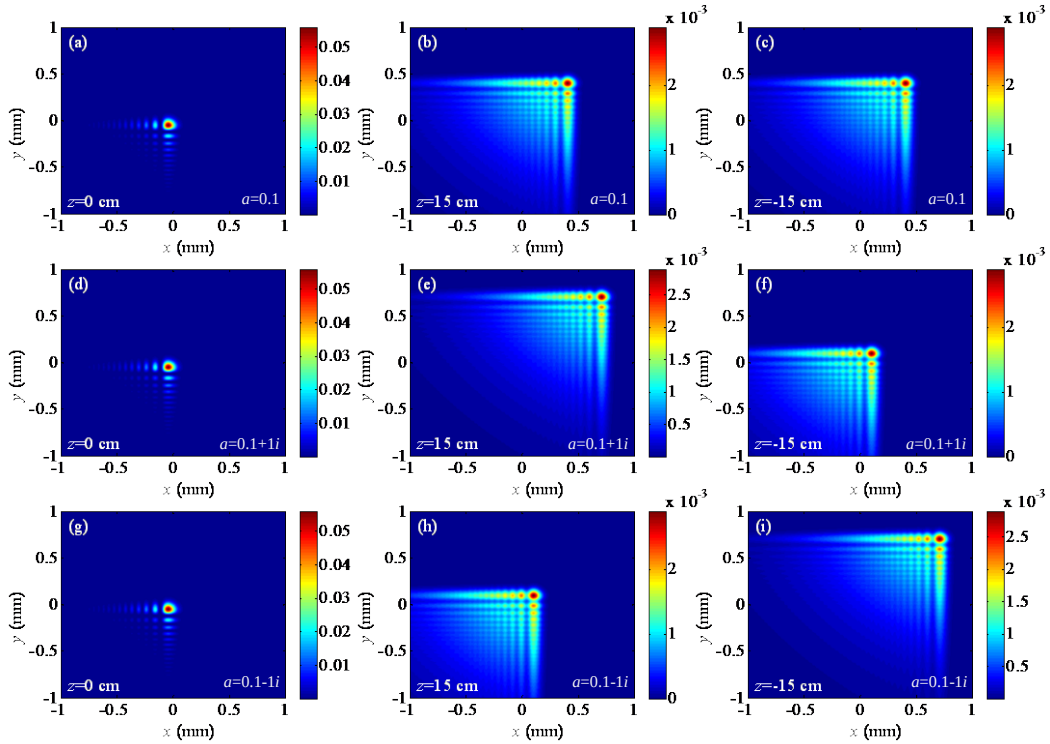

Figure 3.9 Intensity distributions of the (2+1)D finite power Airy beams with three cases of *a*: (1) 0.1 at (a) *z*=0 cm, (b) *z*=15 cm and (c) *z*=-15 cm. (2) 0.1+1*i* at (d) *z*=0 cm, (e) *z*=15 cm and (f) *z*=-15 cm. (3) 0.1-1*i* at (g) *z*=0 cm, (h) *z*=15 cm and (i) *z*=-15 cm.

The images of the finite power Airy beams with *a*=0.1 were captured by the CCD from *z*=-15 cm to *z*=15 cm at the interval of 5 cm as shown in Figs. 3.10(a) - 10(g). They have the similar intensity distributions under the same propagating distance to the +*z*-direction or the -*z*-direction. As a result, the ballistic trajectory is formed during propagation.

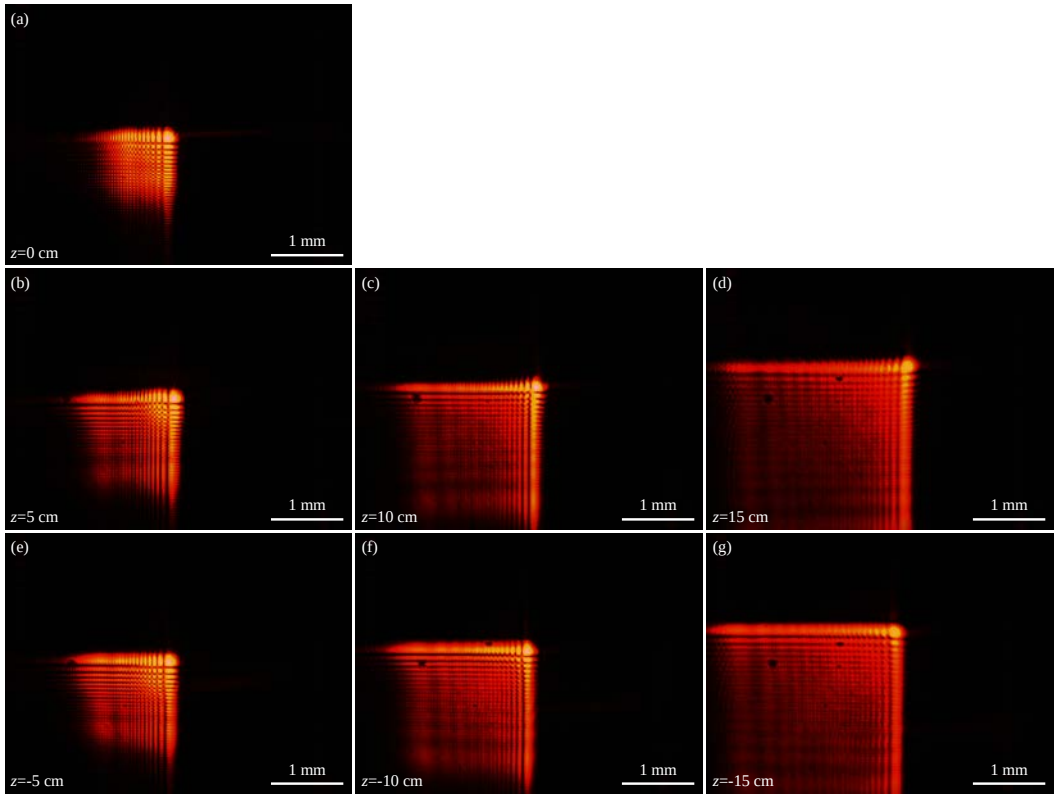

Figure 3.10 Captured CCD images of the (2+1)D finite power Airy beams with a=0.1 from z=-15 cm to z=15 cm at the interval of 5 cm.

In case of a=0.1+1i, the images of the finite power Airy beams were presented from z=-15 cm to z=15 cm at the interval of 5 cm in Figs. 3.11(a) - 11(g). Due to the positive initial launch angle, deflection extents in the +z-direction are longer than that in the -z-direction. Especially, in comparison with Figs. 3.11(d) and 3.11(g), a decided intensity distribution difference originated from more bent trajectory in the +z-direction is shown.

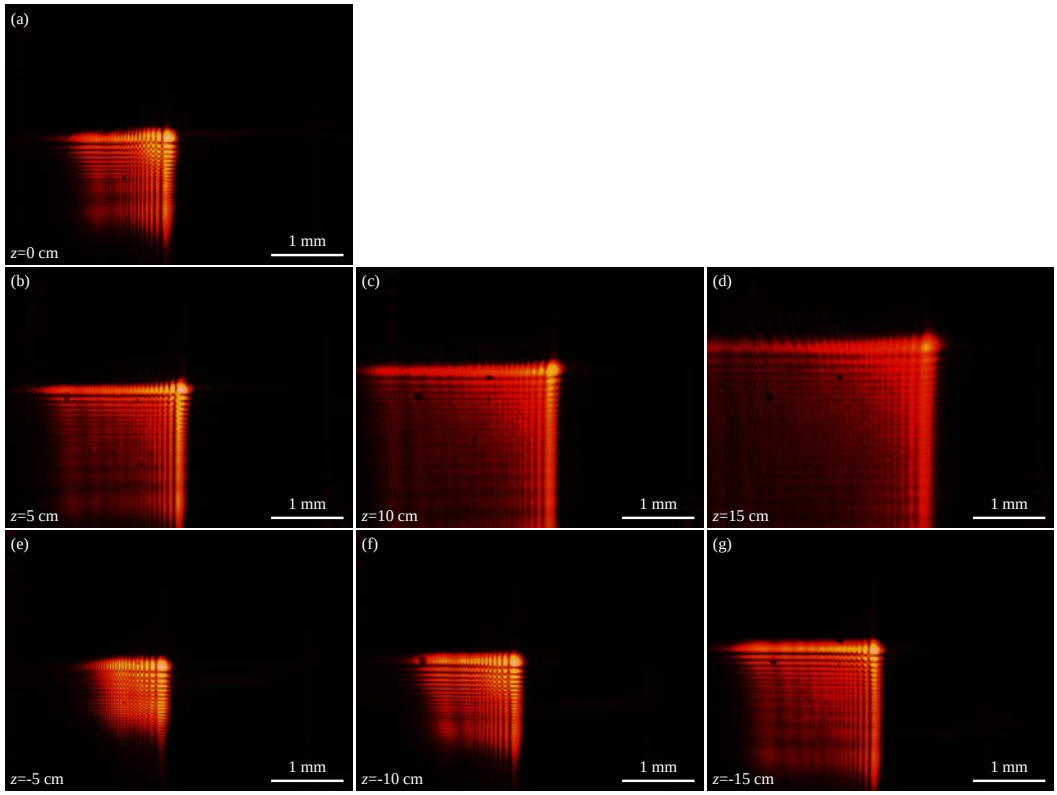

Figure 3.11 Captured CCD images of the (2+1)D finite power Airy beams with a=0.1+1i from z=-15 cm to z=15 cm at the interval of 5 cm.

Finally, when a=0.1-1i, I obtained the CCD images of the finite power Airy beams with the negative initial launch angle case from z=-15 cm to z=15 cm at the interval of 5 cm as shown in Figs. 3.12(a) - 3.12(g). On the contrary to the positive initial launch angle case, deflection extents in the -z-direction are longer than that in the +z-direction. All experimental results coincide well with the calculation results shown in Figs. 3.9(a) - 3.9(i).

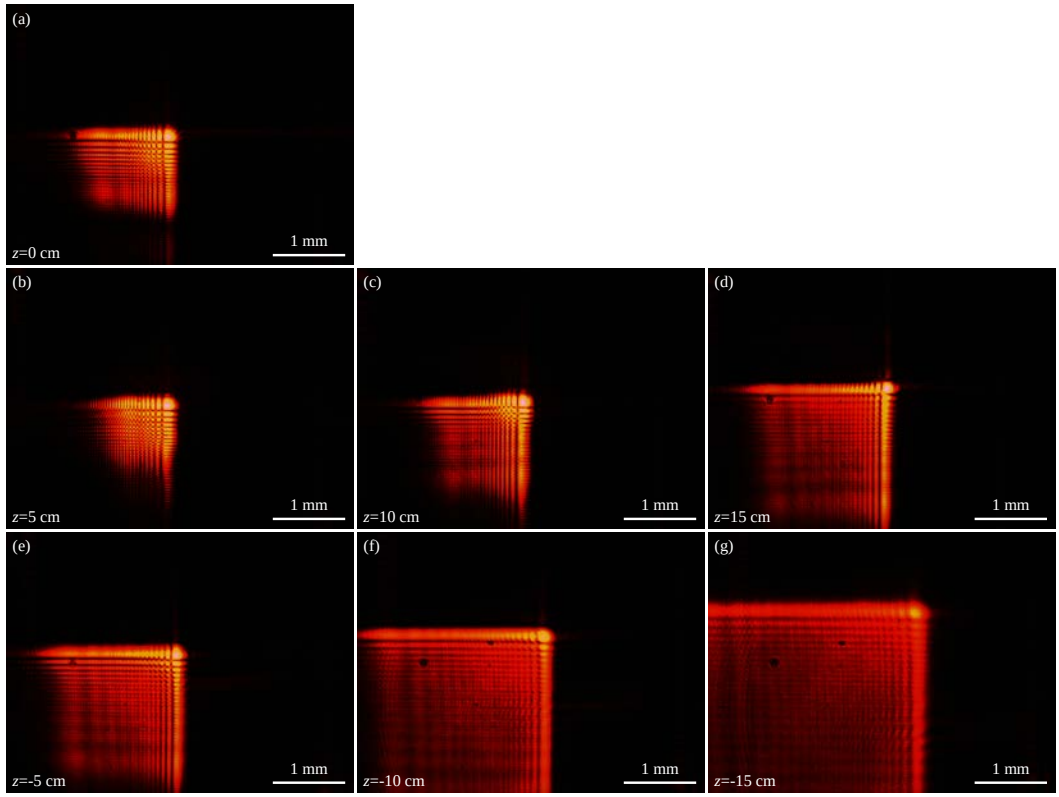

Figure 3.12 Captured CCD images of the (2+1)D finite power Airy beams with a=0.1-1i from z=-15 cm to z=15 cm at the interval of 5 cm.

In the reconstruction procedure, the object beam can also be reconstructed by illuminating the conjugated reference beam U_r^*. In this case, resultant reconstructed wave ϕ_r^* is expressed as below:

$$\phi_r^* = tU_r^* \propto t_o U_r^* + I_r U_r^* + \phi \left| U_r^* \right|^2 + \phi^* I_r . \tag{3.13}$$

In Eq. (3.13), the fourth term $\phi^* I_r$ represents the (2+1)D finite power Airy beams multiplied by the reference beam intensity I_r propagating in the -z-direction. Thus, the phase-conjugated reference beam to reconstruct the conjugated Airy beams which have opposite power flows to the signal Airy beams is considered [58]. When a=0.1+1i, the ballistic trajectory of the reconstructed Airy beams is interesting. From Eq. (3.13), reconstructed Airy beams by the phase-conjugated reference beam can be regarded as the

conjugated Airy beams which mean the Airy beams with a=0.1-1i propagating in the -z-direction. As a result, two Airy beams with the same trajectories and the reversed propagation directions each other can be obtained simultaneously by illuminating the reference beam and the phase-conjugated reference beam. That is, more bent symmetric Airy beams shown in Fig. 3.13 can be generated.

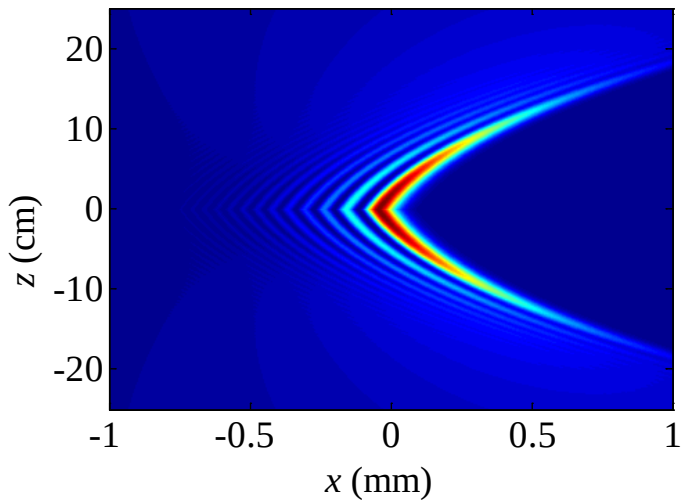

Figure 3.13 Propagation dynamic of more bent symmetric Airy beams.

The schematic diagram of generating the phase-conjugated reference beam is illustrated in Fig 3.14. Suppose that interference patterns between the (2+1)D finite power Airy beams with the initial launch angle of a=0.1+1i and the reference beam with the incident angle of 60° are recorded on the photopolymer placed at z=0 cm. The shifted cubic phase mask (Fig. 3.15) of a=0.1+1i and x_0=y_0=50 μm is used to generate the (2+1)D Airy beams with initial launch angle. While the signal Airy beams are being blocked, the reference beam is illuminating the photopolymer. As a result, the more bent finite power Airy beams propagating in the +z-direction are obtained at z=5 cm, z=10 cm and z=15 cm, which are shown in Figs. 3.16(a), 3.16(b) and 3.16(c), respectively. Blue line represents the position of the main lobe at z=5 cm.

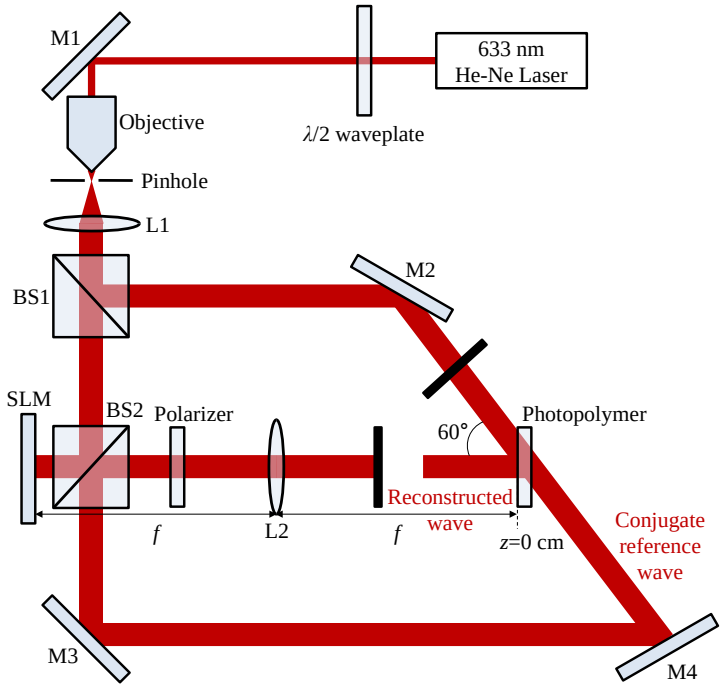

Figure 3.14 Schematic diagrams of reconstruction procedure with conjugated reference beam.

To reconstruct the conjugated Airy beam, the phase-conjugated reference beam illuminates the back side of the photopolymer while both the reference beam and the signal Airy beams are being blocked. In this case, the conjugated Airy beam can be reconstructed to the -*z*-direction. Since Airy beams propagating in the -*z*-direction cannot be generated by the typical generation method using the SLM, the holographic generation method is advantageous to apply to variety of experimental conditions. The CCD camera is placed between L2 and the photopolymer to capture the images of the reconstructed wave. The CCD images of Airy beams at *z*=-5 cm, *z*=-10 cm and *z*=-15 cm are captured and shown in Figs. 3.16(d), 3.16(e) and 3.16(f), respectively. Comparing Figs. 3.16(a) and 3.16(d), there are misalignments among the positions of the initial main lobes. This is originated from the position of the CCD camera. However, they show the approximately same extent of ballistic deflection from each initial position. Therefore, the phase-conjugated reference beam reconstructs the recorded field which has the

reversed propagation direction, keeping its original amplitudes and phases. As a result, more bent symmetric Airy beams are realized experimentally.

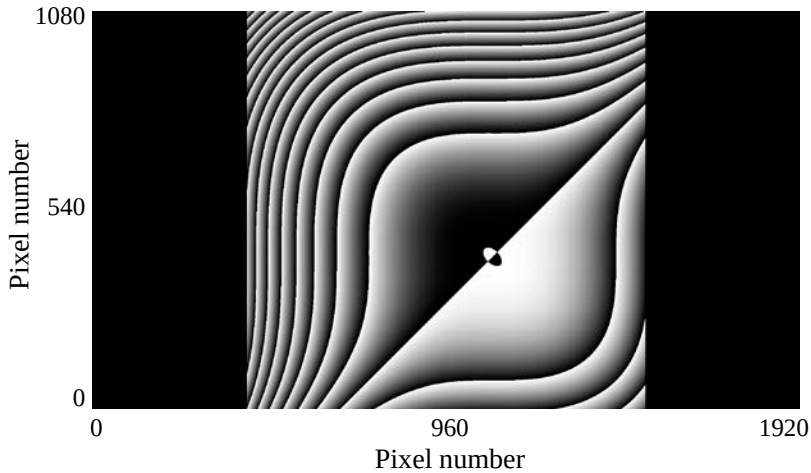

Figure 3.15 Phase mask for launching (2+1)D Airy beams with the initial launch angle: x_0=50 μm, y_0=50 μm and a=0.1+1i.

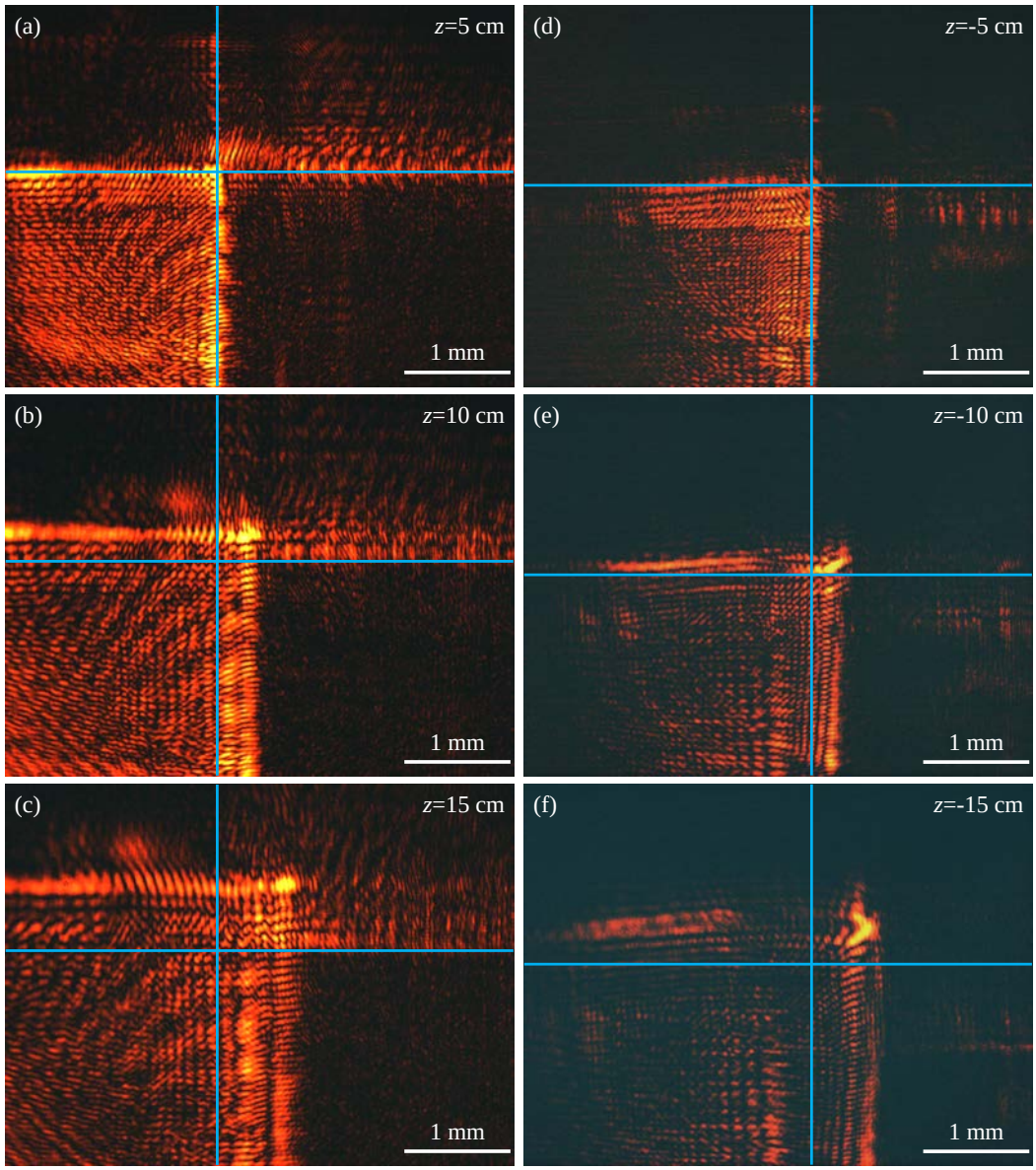

Figure 3.16 Captured CCD images of the reconstructed Airy beams with a=0.1+1i (a) at z=5 cm, (b) z=10 cm and (b) z=15 cm. Captured CCD images of the conjugated Airy beams (a) at z=-5 cm, (b) z=-10 cm and (b) z=-15 cm. Blue line represents the position of the main lobe at z=5 cm.

3.2. Angle multiplexing of Airy beams

In this section, angle multiplexing of two Airy beams determined by the angles of reference beams for practical uses such as optical signal processing, particle tweezers and particle clearing is presented. This work consists of three stages. The first procedure of the first stage is recording the interference patterns of two optical fields which are Airy beams and a plane wave with an incident angle θ on a photopolymer. The second is over-recording the interference patterns between other Airy beams and a plane wave with an incident angle $-\theta$ on the same photopolymer. During the reconstruction procedure, two kinds of reference beams which have the incident angles θ and $-\theta$, respectively, are used. They can be reconstructed both simultaneously and separately.

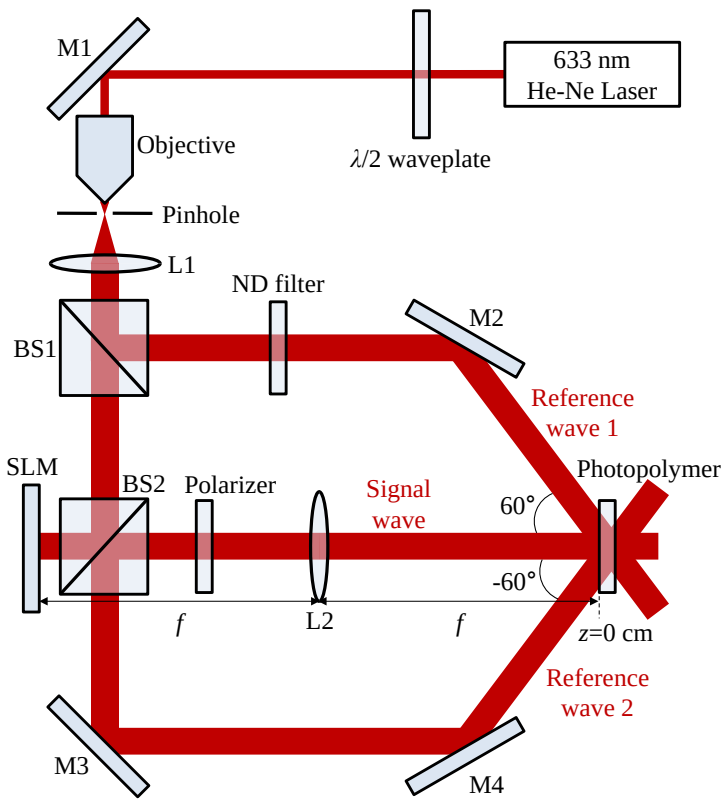

Figure 3.17 Schematic diagrams of recording of Airy beam multiplexing. (M: mirror, L: lens, BS: beam splitter)

3.2.1. Recording of multiple Airy beams

The feasibility of the angle multiplexing of Airy beams based on holography is investigated. In this case, the recording procedure is conducted in twice. Figure 3.17 is a schematic diagram of the recording procedure for the angle multiplexing. Each Airy beam which propagates in different directions of deflection is successively recorded at the same area on the photopolymer. Both reference beams are incident to the photopolymer with 60° and -60° incidence angles and 32 mJ/cm^2 energy density with 40 seconds exposure time. To compensate power difference between reference wave 1 and reference wave 2, a neutral density (ND) filter is located in the reference arm 1. First, the (2+1)D finite power Airy beam with x_0=50 μm and y_0=50 μm (phase mask 1; Fig. 3.3(a)) is recorded on the photopolymer while opening the reference wave 1 and blocking the reference wave 2. Next, the (2+1)D finite power Airy beam with x_0=-50 μm and y_0=-50 μm (phase mask 2; Fig. 3.3(b)) is recorded in the same area of the photopolymer while opening the reference wave 2 and blocking the reference wave 1.

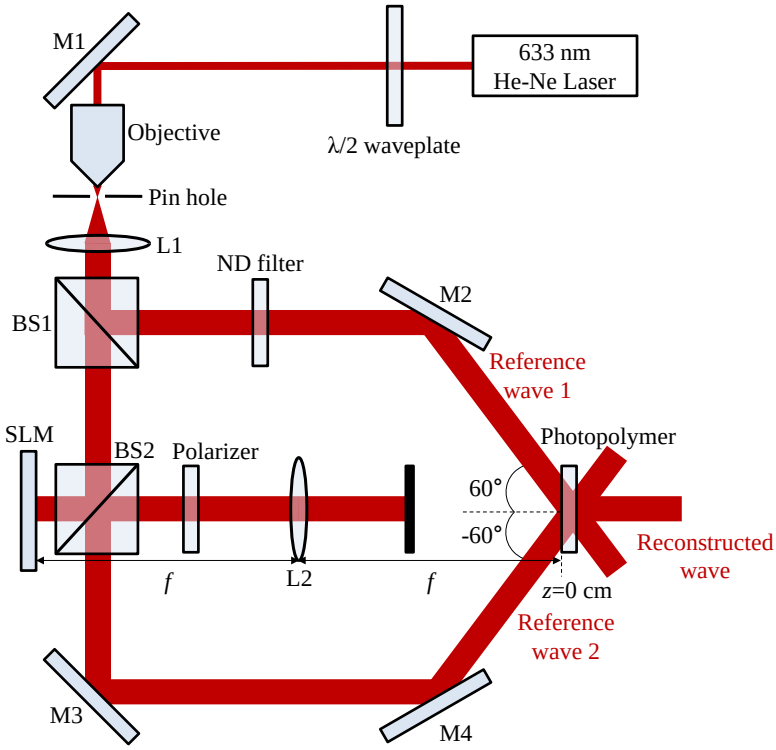

Figure 3.18 Schematic diagrams of reconstruction of Airy beam multiplexing.

3.2.2. Reconstruction of multiple Airy beams

To reconstruct recorded Airy beams, an additional barrier to block the Airy beams between the lens and the photopolymer shown in Fig. 3.18 is used. An experimental setup is also provided in Fig. 3.19. Two reference beams are incident to the photopolymer with 60° and -60° angle at the same time. As a result, two Airy beams accelerating in opposite directions shown in Figs. 3.20(a) and 3.20(b) which are captured at z=5 cm and z=15 cm by the CCD, respectively, are obtained. In Fig. 3.20(b), dual Airy beams which have a symmetric intensity pattern and better self-healing property are shown [59].

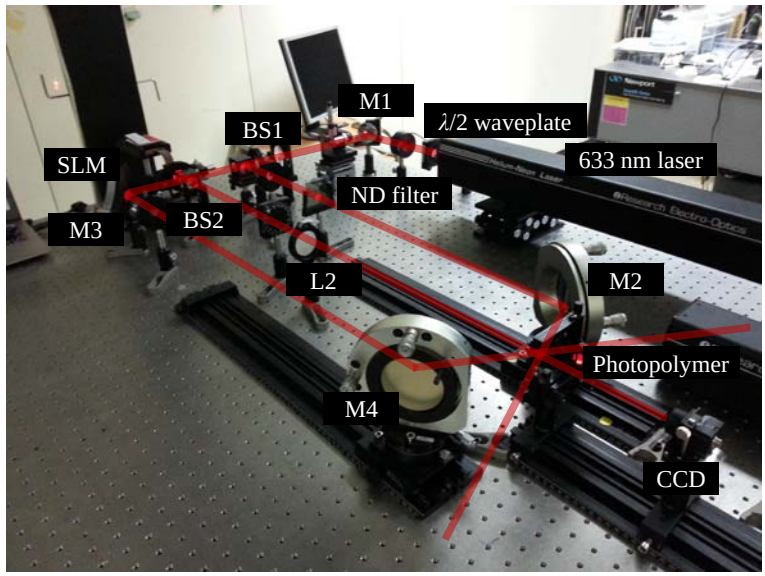

Figure 3.19 Experimental setup of Airy beam multiplexing.

Moreover, only the reference beam 1 is blocked and the CCD images are captured at z=5 cm and z=15 cm as shown in Figs. 3.20(c) and 3.20(d), respectively. In this case, only one Airy beam with x_0=-50 μm and y_0=-50 μm is generated. That is, each Airy beam can be individually controlled when one of the reference beams except one is blocked by a barrier. This can be utilized to on-off switching or routing in optical signal processing [60]. Also, it is possible to adopt particle manipulation: a portion of particles can be held or released while the others are being released or held.

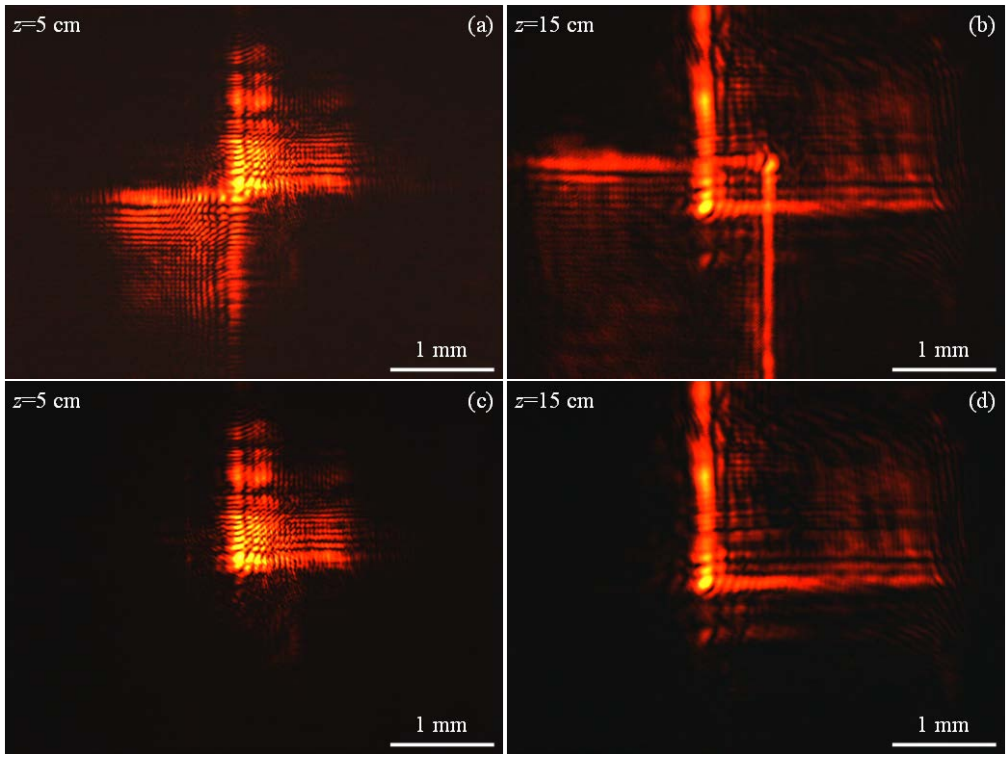

Figure 3.20 Captured CCD images of the reconstructed two Airy beams accelerating in opposite directions, resulted from angle multiplexing (a) at z=5 cm and (b) z=15 cm. Reconstructed Airy beams at (c) z=5 cm and (d) z=15 cm while the reference beam 1 is blocked.

Chapter 4.

Plasmonic approach to Airy beam generation using subwavelength slit array

In this chapter, I present the novel method to launch the finite power Airy beams in free space using a metallic slit array. To set the initial phase distribution and the intensity profile of the finite power Airy beams, it is divided into seven sections according to the seven lobes. In each section, the number of slits and the slit height determine the intensity and the phase, respectively. The launched beams have the properties of the Airy beams: diffraction-free, bending and self-regeneration. I expect that this method can be utilized to generate various beams which have the desired initial phase and intensity profiles without the use of any complicated optical components and to manipulate nanoparticles, being adopted in optical tweezing and trapping.

4.1. Design of subwavelength metallic slit array

I propose a new method which can launch the Airy wave packet based on the metallic slit array. It is widely known that the light manipulation such as beaming and focusing can be realized by controlling surface plasmon polartons (SPPs) excited at the exit of the subwavelength slit [61-65]. Especially, a properly designed slit array which plays a role of a lens can build up the highly directional beam or the focused beam determined by phase retardations between adjacent slits [61, 62]. From the Huygens' principle,

diffracted light came from each slit end acts as an individual point source and the interference of the spherical waves makes specific interference patterns. I adopt this mechanism on the Airy beam generation instead of the complicated generation systems. The two requisites for the Airy beam generation on the initial intensity profile and the phase distribution, can be satisfied just by arranging a metallic slit array. The number of the slits and the slit height can control the intensity and the phase retardation, respectively.

4.1.1. Metal-insulator-metal plasmonic waveguide

Throughout this chapter, I regard each subwavelength metallic slit as the metal-insulator-metal (MIM) waveguide. The MIM waveguide is composed of the dielectric core and surrounding metal claddings [6]. In the MIM waveguide, the SPP modes are strongly confined at the metal-dielectric interfaces because the tails of the SPP wave cannot penetrate deep into the surrounding metal claddings. The MIM waveguide can support two sorts of the SPP modes which are the symmetric mode and the anti-symmetric mode. Supposing *p*-polarized light propagates along the *z*-direction in the MIM waveguide, only E_x, E_z and H_y components of electromagnetic fields can exist. I describe the symmetric and anti-symmetric plasmonic modes of the *y*-component magnetic field H_y in the MIM waveguide with its width of the insulator part (w) as follows:

$$H_y(x,z;t)=\begin{cases} A_1\exp\left[-k_m\left(x-\frac{w}{2}\right)\right]\exp\left[j\left(\beta z-\omega t\right)\right] & \left(x\geq\frac{w}{2}\right) \\ B_1\cosh\left(k_d x\right)\exp\left[j\left(\beta z-\omega t\right)\right] & \left(-\frac{w}{2}\leq x\leq\frac{w}{2}\right) \\ A_1\exp\left[k_m\left(x+\frac{w}{2}\right)\right]\exp\left[j\left(\beta z-\omega t\right)\right] & \left(x\leq-\frac{w}{2}\right) \end{cases} \tag{4.1}$$

and

$$H_y(x,z;t)=\begin{cases} A_2\exp\left[-k_m\left(x-\dfrac{w}{2}\right)\right]\exp\left[j\left(\beta z-\omega t\right)\right] & \left(x\geq\dfrac{w}{2}\right) \\ B_2\sinh\left(k_d x\right)\exp\left[j\left(\beta z-\omega t\right)\right] & \left(-\dfrac{w}{2}\leq x\leq\dfrac{w}{2}\right) \\ -A_2\exp\left[k_m\left(x+\dfrac{w}{2}\right)\right]\exp\left[j\left(\beta z-\omega t\right)\right] & \left(x\leq-\dfrac{w}{2}\right), \end{cases} \tag{4.2}$$

where β is the propagation constant in the MIM waveguide. k_m and k_d represent wavenumbers in metal and dielectric, respectively. By momentum conservation relation, I obtain

$$\beta^2=k_m^2+\varepsilon_m^2k_0^2=k_d^2+\varepsilon_d^2k_0^2, \tag{4.3}$$

where k_0 is a wavenumber of the incident light in free space. In addition, x- (E_x) and z- (E_z) component electric fields of the symmetric and anti-symmetric plasmonic modes are derived from the following Maxwell's curl equation:

$$E_x=-\frac{1}{j\omega\varepsilon_0\varepsilon_r}\left(-\frac{\partial H_y}{\partial z}\right) \tag{4.4}$$

and

$$E_z=-\frac{1}{j\omega\varepsilon_0\varepsilon_r}\left(\frac{\partial H_y}{\partial x}\right). \tag{4.5}$$

First, E_x and E_z of the symmetric plasmonic mode is expressed as below:

$$E_x(x,z;t)=\begin{cases} \left(\dfrac{\beta}{\omega\varepsilon_0\varepsilon_m}\right)A_1\exp\left[-k_m\left(x-\dfrac{w}{2}\right)\right]\exp\left[j\left(\beta z-\omega t\right)\right] & \left(x\geq\dfrac{w}{2}\right) \\ \left(\dfrac{\beta}{\omega\varepsilon_0\varepsilon_d}\right)B_1\cosh\left(k_d x\right)\exp\left[j\left(\beta z-\omega t\right)\right] & \left(-\dfrac{w}{2}\leq x\leq\dfrac{w}{2}\right) \\ \left(-\dfrac{\beta}{\omega\varepsilon_0\varepsilon_m}\right)A_1\exp\left[k_m\left(x+\dfrac{w}{2}\right)\right]\exp\left[j\left(\beta z-\omega t\right)\right] & \left(x\leq-\dfrac{w}{2}\right) \end{cases} \tag{4.6}$$

and

$$E_z(x,z;t)=\begin{cases}\left(\dfrac{k_m}{j\omega\varepsilon_0\varepsilon_m}\right)A_1\exp\left[-k_m\left(x-\dfrac{w}{2}\right)\right]\exp\left[j(\beta z-\omega t)\right] & \left(x\ge\dfrac{w}{2}\right)\\ \left(-\dfrac{k_d}{\omega\varepsilon_0\varepsilon_d}\right)B_1\sinh(k_d x)\exp\left[j(\beta z-\omega t)\right] & \left(-\dfrac{w}{2}\le x\le\dfrac{w}{2}\right)\\ \left(\dfrac{k_m}{j\omega\varepsilon_0\varepsilon_m}\right)A_1\exp\left[k_m\left(x+\dfrac{w}{2}\right)\right]\exp\left[j(\beta z-\omega t)\right] & \left(x\le-\dfrac{w}{2}\right),\end{cases} \quad (4.7)$$

respectively. Next, E_x and E_z of the anti-symmetric plasmonic mode is expressed as below:

$$E_x(x,z;t)=\begin{cases}\left(\dfrac{\beta}{\omega\varepsilon_0\varepsilon_m}\right)A_2\exp\left[-k_m\left(x-\dfrac{w}{2}\right)\right]\exp\left[j(\beta z-\omega t)\right] & \left(x\ge\dfrac{w}{2}\right)\\ \left(\dfrac{\beta}{\omega\varepsilon_0\varepsilon_d}\right)B_2\sinh(k_d x)\exp\left[j(\beta z-\omega t)\right] & \left(-\dfrac{w}{2}\le x\le\dfrac{w}{2}\right)\\ \left(-\dfrac{\beta}{\omega\varepsilon_0\varepsilon_m}\right)A_2\exp\left[k_m\left(x+\dfrac{w}{2}\right)\right]\exp\left[j(\beta z-\omega t)\right] & \left(x\le-\dfrac{w}{2}\right)\end{cases} \quad (4.8)$$

and

$$E_z(x,z;t)=\begin{cases}\left(\dfrac{k_m}{j\omega\varepsilon_0\varepsilon_m}\right)A_2\exp\left[-k_m\left(x-\dfrac{w}{2}\right)\right]\exp\left[j(\beta z-\omega t)\right] & \left(x\ge\dfrac{w}{2}\right)\\ \left(-\dfrac{k_d}{\omega\varepsilon_0\varepsilon_d}\right)B_2\cosh(k_d x)\exp\left[j(\beta z-\omega t)\right] & \left(-\dfrac{w}{2}\le x\le\dfrac{w}{2}\right)\\ \left(\dfrac{k_m}{j\omega\varepsilon_0\varepsilon_m}\right)A_2\exp\left[k_m\left(x+\dfrac{w}{2}\right)\right]\exp\left[j(\beta z-\omega t)\right] & \left(x\le-\dfrac{w}{2}\right),\end{cases} \quad (4.9)$$

respectively. From Eqs. (4.1), (4.6) and (4.7), coupling coefficients A_1 and B_1 are obtained as below:

$$A_1=B_1\cosh\left(k_d\frac{w}{2}\right) \quad (4.10)$$

and

$$\frac{k_m}{\varepsilon_m}A_1=-\frac{k_d}{\varepsilon_d}B_1\sinh\left(k_d\frac{w}{2}\right). \quad (4.11)$$

As a result, the dispersion relation of the symmetric mode of the MIM waveguide is

$$\frac{k_m}{\varepsilon_m}+\frac{k_d}{\varepsilon_d}\tanh\left(k_d\frac{w}{2}\right)=0. \tag{4.12}$$

In like manner, from Eqs. (4.2), (4.8) and (4.9), relations of coupling coefficients A_2 and B_2 are obtained as below:

$$A_2=B_2\sinh\left(k_d\frac{w}{2}\right) \tag{4.13}$$

and

$$\frac{k_m}{\varepsilon_m}A_2=-\frac{k_d}{\varepsilon_d}B_2\cosh\left(k_d\frac{w}{2}\right). \tag{4.14}$$

As a result, the dispersion relation of the anti-symmetric mode of the MIM waveguide is

$$\frac{k_m}{\varepsilon_m}+\frac{k_d}{\varepsilon_d}\coth\left(k_d\frac{w}{2}\right)=0. \tag{4.15}$$

4.1.2. Design of subwavelength metallic slit array

There are two surface plasmon modes in the MIM waveguide which are the symmetric mode and anti-symmetric mode according to the *y*-component of the magnetic field distribution. In this chapter, let me consider only the symmetric mode since the anti-symmetric mode exhibits the cut-off process as the dielectric core width is decreased below hundreds of nanometers [66]. From solving the Maxwell's equations where tangential components of the electric field and magnetic field should be continuous at the boundaries between different media, the dispersion relation in the TM polarization, Eq. (4.12) combining with Eq. (4.3) is rewritten as below:

$$\tanh\left(\frac{w}{2}\sqrt{\beta^2-k_0^2\varepsilon_d}\right)=-\frac{\varepsilon_d\sqrt{\beta^2-k_0^2\varepsilon_m}}{\varepsilon_m\sqrt{\beta^2-k_0^2\varepsilon_d}}, \tag{4.16}$$

Throughout this chapter, permittivity values of metal ε_m and dielectric are -10.1889+0.8311*i* [68] and 1, respectively, when operation wavelength is 532 nm. Figures 4.1(a) and (b) show

relations of the real part and imaginary part of effective index n_{eff} as a function of the slit width w. According to Eq. (4.16) or Fig. 4.1(a), the real part of effective index n_{eff} ($=\beta/k_0$) of the subwavelength slit continues decreasing as the slit width w is increased. In addition, the imaginary part of effective index also shows the same tendency from Fig. 4.1(b).

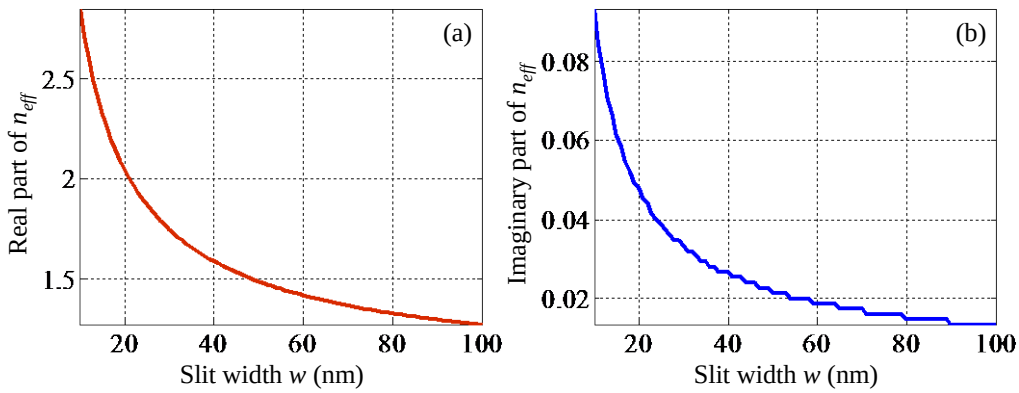

Figure 4.1 (a) Real part and (b) imaginary part of effective index as a function of the slit width w in the MIM waveguide.

After passing through the subwavelength metallic slit (MIM waveguide), the SPP mode undergoes the phase retardation as much as $\Delta\varphi$ which can be expressed by the following equation [61]:

$$\Delta\varphi = \mathrm{Re}(\beta h) + \arg\left[1 - \left(\frac{1-\beta/k_0}{1+\beta/k_0}\right)^2 \exp(2i\beta h)\right], \tag{4.17}$$

where h is the slit height. In general, the second argument term of Eq. (4.17) is omitted because it is small compared with the first term $\mathrm{Re}(\beta h)$. Combining Eqs. (4.16) and (4.17), it is known that the slit width w determines the propagation constant β and the phase retardation $\Delta\varphi$ is a function of the slit height h with the fixed propagation constant β. When the silt widh w is fixed as 50 nm, the phase retardation $\Delta\varphi$ as a function of slit hetght h is plotted in Fig. 4.2. Here, $\Delta\varphi$ is given as zero when h is 100 nm.

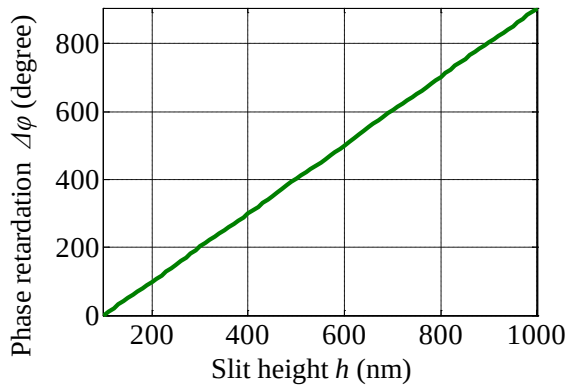

Figure 4.2 Phase retardation $\Delta\varphi$ as a function of the slit height h with fixed w (=50 nm).

4.2. Numerical simulations and results

In this chapter, numerical simulations are conducted by COMSOL Multiphysics, which is based on the finite elements method (FEM) [67]. Here, the FEM is a numerical simulation technique used to solving a variety of the scientific and engineering analysis based on partial differential equations. It is advantageous to apply the arbitrary points or shapes in an analytic domain. Moreover, it can easily approach to the geometrically complicated structure, nonlinear medium and anisotropic material.

To perform the precise FEM simulation, dense triangular meshes are used. It is necessary to balance between overflows of the computer memory and smaller mesh size. In theses simulations, the waveguide domains around the skin depth of SPP which is about 50 nm in this case are divided into many triangular FEM meshes. Above all, meshes of slit boundaries are set to be 50 nm, which is sufficiently dense when compared with operation wavelength of incident light.

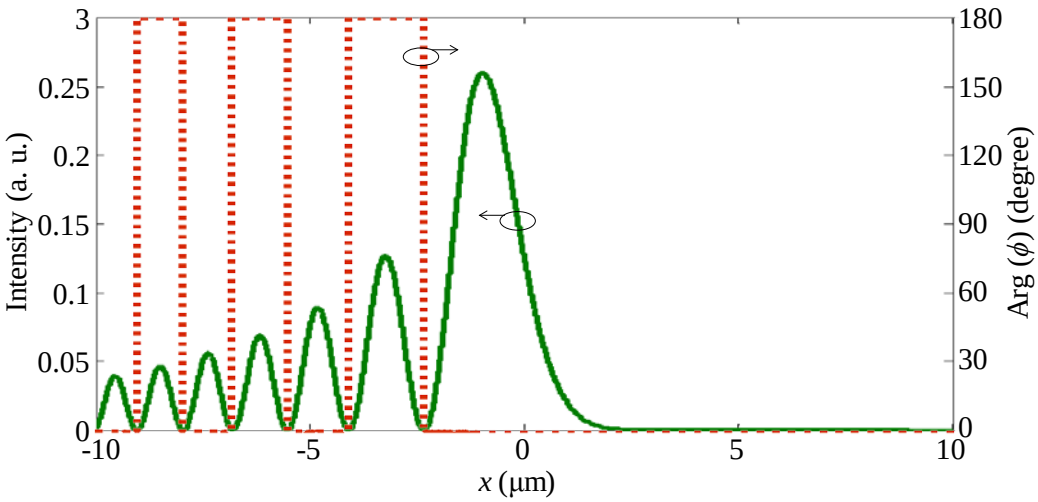

Figure 4.3 At the input (z=0 μm), the cross-section of intensity distributions (solid green line) and the phase distribution of the finite power Airy beams are shown in case of a=0.05, x_0=1 μm and λ=532 nm.

4.2.1. Numerical simulation of Airy beam generation

Throughout this chapter, a=0.05, x_0=1 μm and λ=532 nm are assumed. At the input (z=0), the cross-section of intensity profile and the phase distribution are plotted in Fig. 4.3. The intensity profile has the highest value at the main lobe spanned between -2.34 μm and 10 μm and it is sinusoidally decreased to the side lobes while the phases are periodically changed between 0° and 180° from the main lobe to the side lobes. Figure 4.4 is a schematic diagram of the proposed structure for launching the finite power Airy beams. It consists of a sliver (Ag) slab (ε_m=-10.1889+0.8311i at 532 nm wavelength) with a metallic slit array which is filled with air (ε_d=1). In case of slit width w (=50 nm) which is fixed throughout this chapter, the real part of the effective index Re(n_{eff}) is calculated as 1.4856 from the transfer matrix method (TMM). When p-polarized light is incident to the bottom of the Ag slab, light is coupled into SPPs at each slit. After propagating along the slits, SPPs are coupled into light again at the slit ends. Diffracted light at each slit end is regarded as an individual point source which radiates a spherical wave into free space with the initial phase and transmittance. From the Huygens' principle, the point sources

started from slit ends make the interference patterns which form the arbitrary shapes in free space.

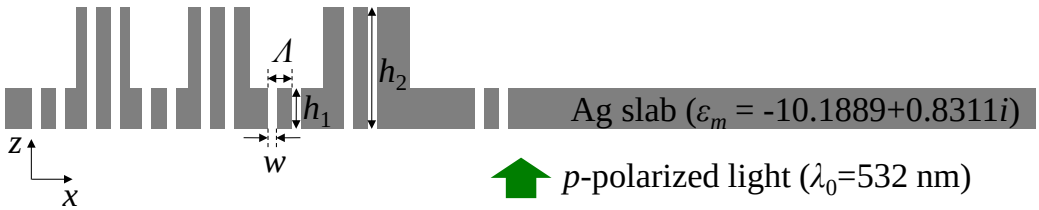

Figure 4.4 Schematic diagram of the proposed structure for launching the finite power Airy beams.

Design rule is as follows. The Ag slab is divided into seven sections. Each section is one-to-one correspondence to each lobe of the finite power Airy beams which is truncated to seven lobes. The structural parameters of the proposed structure are designed to achieve the initial conditions of the finite power Airy beams (Fig. 4.3) at 2 μm apart from the bottom of the Ag slab which is a sufficient distance to separate surface plasmon wave and diffracted spherical wave. To make 180° phase difference between adjacent sections, the Ag slab has stepped-heights denoted by h_1 and h_2. To fit the shape of the intensity profile, the number of slits is assumed: the transmittance from the multiple slits is the linear summation of the single slit transmittance and the more number of the slits is, the stronger transmittance can be achieved. Since the extraordinary transmission and the zero transmission do not occur in the designed grating width (w=50 nm) and grating period (Λ=150 nm), these assumptions can be acceptable [69,70]. Figure 4.5 shows transmitted power as a function of the slit height h obtained by the FEM method when p-polarized light with 532 nm is incident to a single slit with 50 nm width. Here, the transmittance power after passing through a single slit is calculated by the line integral at 2 μm apart from the bottom of the slit. It is periodically increased and decreased while the slit height h is being increased due to the Fabry-Pérot resonance. If the area of the main lobe is set to 100, the area ratio among the lobes in Fig. 4.3 is 100 : 49 : 34 : 27 : 22 : 18 : 15. In this thesis, h_1 and h_2 are selected to 339 nm and 883 nm because they satisfy not only the 180° phase difference calculated from Eq. (4.17) but also have the

transmitted power ratio of roughly 10 : 7. When the transmitted power ratio between h_1 and h_2 is 10 : 7, the difference between the area ratio and the intensity ratio determined by slit number is comparatively less. In this case, the numbers of the metallic slits in each section are selected to 14 (=h_1), 9 (=h_2), 5 (=h_1), 5 (=h_2), 3 (=h_1), 3 (=h_2) and 2 (=h_1), respectively, which make intensity ratio of 100 : 46 : 36 : 26 : 21 : 15 : 4. The slit array is located within the center of the full-width at the half-maximum (FWHM) range.

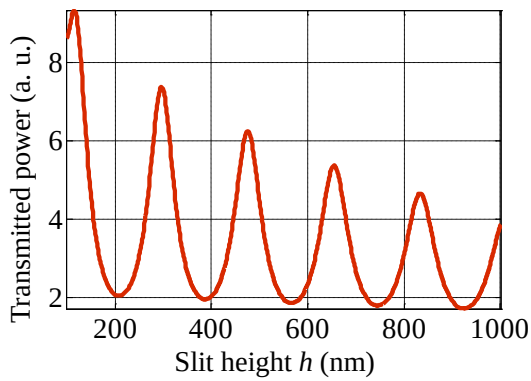

Figure 4.5 Transmitted power after passing through a single slit with 50 nm width as a function of slit height h.

Figure 4.6(a) shows the free space propagation of the finite power Airy beams generated by the proposed structural parameters. Although the slight diffraction patterns appear around slit exits, it clearly shows the bending trajectory to the $+x$ direction with non-diffraction. To compare generated Airy beams with calculated Airy beams, the calculated (1+1)D finite power Airy beams in case of a=0.05, x_0=1 μm and λ=532 nm are presented in Fig. 4.6(b). Both cases show very similar propagation behaviors. However, since the number of the slits should be an integer, it is difficult to set the exact area ratio by just the number of the slits. For this reason, slight diffraction is an inevitable consequence, compared with the calculated case.

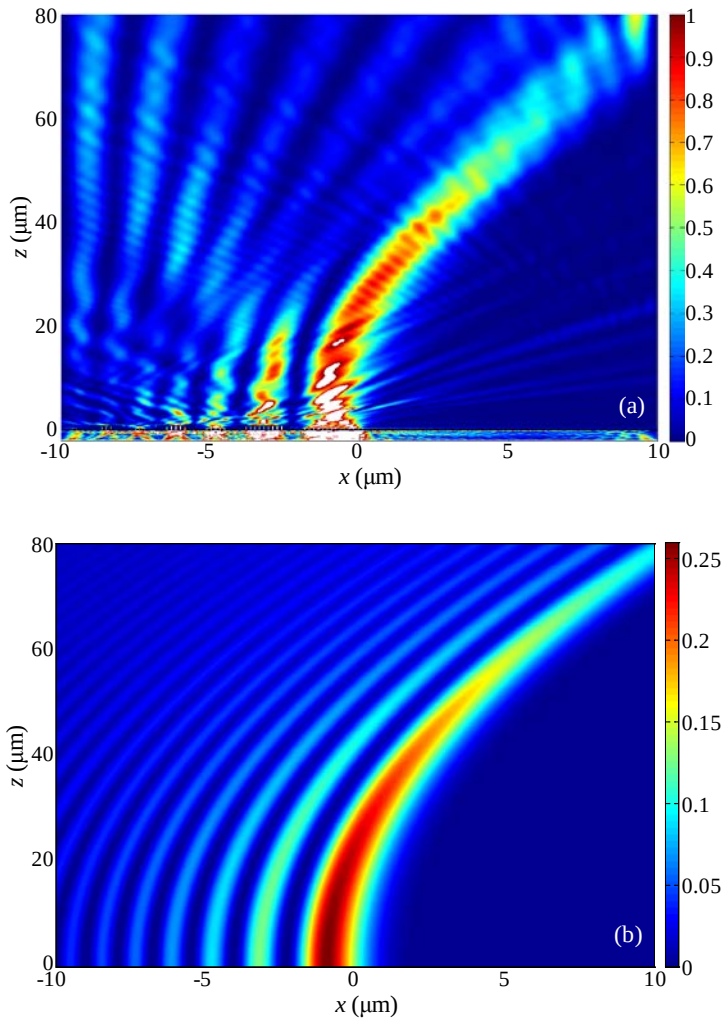

Figure 4.6 (a) Intensity distribution of the (1+1)D finite power Airy beams generated by the metallic slit array with h_1=339 nm and h_2=883 nm. (b) Free space propagation of the calculated (1+1)D finite power Airy beams in case of a=0.05, x_0=1 μm and λ=532 nm.

4.2.2. Self-healing property in Airy beams

If a part of Airy beams is blocked by an opaque obstacle, they can reconstruct their original shapes during propagation. This phenomenon is originated from constructive

interferences of plane waves with adjusting phase along the curve trajectory. To check self-healing property, the propagating path of the main lobe is totally blocked using an opaque metallic obstacle (size: 2 μm × 1 μm) which is positioned 2 μm apart from the slit entrance of the main lobe. As a result, overall intensity is weak but spherical waves radiated from slits of other lobes regenerate the shape of the finite power Airy beams shown in Fig. 4.7(a). Moreover, the propagation dynamics of the finite power Airy beam mode which is incident at the bottom boundary calculated by the FEM technique is presented in Fig. 4.7(b). The white box which denote the opaque metallic obstacle blocks the propagation path of the main lobe in the Airy beams. Similarly, it shows reconstructions of the main lobe and remain their original field distribution in the *x*-direction. This results prove that the proposed structure can generate the Airy beams satisfying the self-healing property.

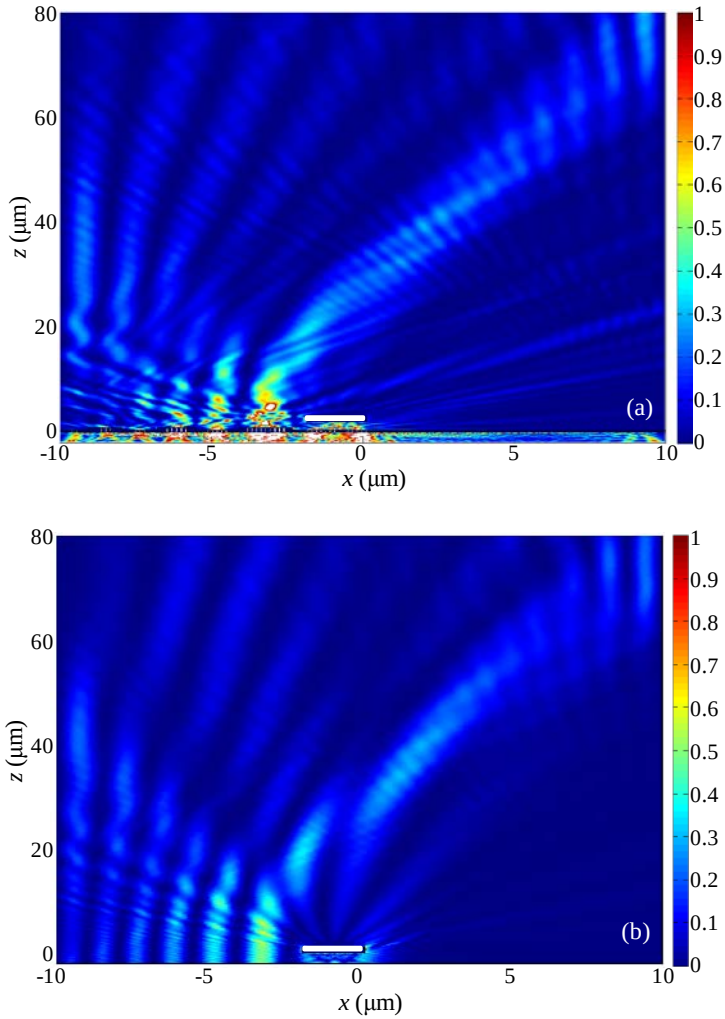

Figure 4.7 Self-healing property in the (1+1)D finite power Airy beams (a) generated by the proposed structure and (b) calculated by the FEM technique. The white box indicates an opaque metallic obstacle which has 2 μm × 1μm size and is located at (-1.855 μm, 2 μm).

Chapter 5.

Conclusion

In this dissertation, novel methods to generate the finite power Airy beams are proposed. Proposed three types of the generation methods are based on initial field modulation, holographic technique and plasmonic approach, respectively. The ballistic trajectory as well as field distributions of the generated Airy beams via theoretical analysis and numerical simulation are analyzed. In addition, experimental results were presented to verify them.

In Chapter 2, based on the initial field modulation, the new types of the finite power Airy beams to solve the diffraction problem originated from realistic constraints were suggested. Total three types of Airy beams generated from a Gaussian beam, a uniform beam of finite extent and an inverse Gaussian beam are theoretically and experimentally investigated. Each finite power Airy beam shows notable propagation dynamics. A uniform beam of finite extent can generate the finite power Airy beam with longer propagation length than that generated by conventional Gaussian beam. The finite power Airy beam generated by an inverse Gaussian beam shows a focused-bending trajectory which is an example proving the self-healing property: side lobes without the main lobe of the Airy beams can reconstruct their Airy profile during the propagation. Therefore, under limiting experimental conditions, using a uniform beam of finite extent is advantageous to generate the finite power Airy beams with less diffraction.

In Chapter 3, the finite power Airy beams using holographic techniques were presented. This method enables simple and robust generation as well as multiplexing of Airy beams. At first, holographic recording and reconstruction procedures allowed to

generate the finite power Airy beams without the conventional system which consists of the SLM and the Fourier lens. In addition, by illuminating the imperfect reference beam which was partially blocked by an obstacle, the self-healing of the Airy beams in the reconstruction procedures is observed. Also, by recording the Airy beams propagating along the asymmetrical trajectory and reconstructing them by the use of the phase-conjugated reference beam, two Airy beams having the same trajectories and the reverse propagation directions to each other were obtained both simultaneously and independently. Based on this experiment, more bent symmetric Airy beams can be generated. Meanwhile, a feasibility study about angle multiplexing of the Airy beams determined by the incident angles of the reference beams is investigated. At first, two Airy beams propagating in the different directions are recorded. Each Airy beam was individually and simultaneously reconstructed when one of the reference beams was blocked by a barrier or all reference beams were opened. This work is suitable to application on on-off switching or routing for optical signal processing. Also, it is possible to adopt particle manipulation: a portion of particles can be held or released while others are held.

In chapter 4, I presented the novel method to launch the finite power Airy beams with compact size using plasmonic structure which consisted of a subwavelength slit array. The designed metallic slit array played a role of the plasmonic lens which determined the transmitted power and the phase retardation of the transmitted surface plasmon mode. At the origin, the finite Airy beams have the intensity distribution with the Airy function profile and the phase distribution of 180° phase difference between adjacent slits. To design the plasmonic structure to launch the finite power Airy beams, we have to determine the number of the slits and slit height which determine intensity and phase retardation of the transmitted wave, respectively. Firstly, the finite power Airy beams were truncated to seven lobes and each lobe was one-to-one correspondence to each subwavelength slit section in the Ag slab. Secondly, transmitted power and phase retardation through a single slit are calculated. Thirdly, using stepped slit heights to satisfy 180° phase difference, slit numbers are selected to close the ratio of lobe areas. Naturally, the launched Airy beams had the same characteristics to those generated by the

conventional method. This work suggested the new generation method not only to solve bulky size of the conventional system but also to reduce high cost of optical components.

Appendix

A.1. Fourier transform of ideal Airy beams

The Airy function which is a solution of wave equation, named by the British astronomer George Biddell Airy (1801 ~ 1892), can be defined by the improper Riemann integral form:

$$Ai(s)=\frac{1}{\pi}\int_0^{\infty}\cos\left(\frac{t^3}{3}+st\right)dt, \tag{A.1}$$

where s and t denote the transverse coordinate and the time. Fourier transform Φ_0 of Eq. (A.1) is expressed as

$$\begin{aligned}
\Phi_0 &= \int_{-\infty}^{\infty} Ai(s)\exp(-jks)ds \\
&= \int_{-\infty}^{\infty}\frac{1}{\pi}\int_0^{\infty}\cos\left(\frac{t^3}{3}+st\right)dt\exp(-jks)ds \\
&= \frac{1}{\pi}\int_0^{\infty}\int_{-\infty}^{\infty}\cos\left(\frac{t^3}{3}+st\right)\exp(-jks)dsdt \\
&= \frac{1}{2\pi}\int_0^{\infty}\int_{-\infty}^{\infty}\left\{\exp\left[j\left(\frac{t^3}{3}+st\right)\right]+\exp\left[-j\left(\frac{t^3}{3}+st\right)\right]\right\}\exp(-jks)dsdt \\
&= \frac{1}{2\pi}\int_0^{\infty}\int_{-\infty}^{\infty}\left\{\exp\left[j\left(\frac{t^3}{3}+st-ks\right)\right]+\exp\left[-j\left(\frac{t^3}{3}+st+ks\right)\right]\right\}dsdt \\
&= \frac{1}{2\pi}\int_0^{\infty}\exp\left(j\frac{t^3}{3}\right)\int_{-\infty}^{\infty}\exp\left[js(t-k)\right]dsdt \\
&+ \frac{1}{2\pi}\int_0^{\infty}\exp\left(-j\frac{t^3}{3}\right)\int_{-\infty}^{\infty}\exp\left[-js(t+k)\right]dsdt \\
&= \frac{1}{2\pi}\int_0^{\infty}\exp\left(j\frac{t^3}{3}\right)2\pi\delta(t-k)dt+\frac{1}{2\pi}\int_0^{\infty}\exp\left(-j\frac{t^3}{3}\right)2\pi\delta(t+k)dt
\end{aligned} \tag{A.2}$$

$$= \frac{1}{2}\exp\left(\frac{j}{3}k^3\right) + \frac{1}{2}\exp\left(-\frac{j}{3}(-k)^3\right)$$
$$= \exp\left(\frac{j}{3}k^3\right).$$

A.2. Fourier transform of finite power Airy beams

The finite power Airy beam solution ϕ_1 is

$$\phi_1(s,\xi) = \mathrm{Ai}\left(s - \left(\frac{\xi}{2}\right)^2 + ia\xi\right)\exp\left(as - \frac{a\xi^2}{2} - i\left(\frac{\xi^3}{12}\right) + i\left(\frac{a^2\xi}{2}\right) + i\left(\frac{s\xi}{2}\right)\right). \quad \text{(A.3)}$$

At the initial position (ξ=0), Eq. (A.3) becomes

$$\phi_1(s,\xi=0) = Ai(s)\exp(as). \quad \text{(A.4)}$$

Fourier transform Φ_1 of Eq. (A.4) is obtained by the same procedures as Eq. (A.2):

$$\Phi_1 = \int_{-\infty}^{\infty} Ai(s)\exp(as)\exp(-j2\pi ks)ds$$
$$= \int_{-\infty}^{\infty}\frac{1}{\pi}\int_0^{\infty}\cos\left(\frac{t^3}{3}+st\right)dt\exp(as-jks)ds$$
$$= \frac{1}{\pi}\int_0^{\infty}\int_{-\infty}^{\infty}\cos\left(\frac{t^3}{3}+st\right)\exp(as-jks)dsdt$$
$$= \frac{1}{\pi}\int_0^{\infty}\int_{-\infty}^{\infty}\cos\left(\frac{t^3}{3}+st\right)\exp(-jKs)dsdt \text{ where } K = k + ja$$
$$= \frac{1}{2\pi}\int_0^{\infty}\int_{-\infty}^{\infty}\left\{\exp\left[j\left(\frac{t^3}{3}+st\right)\right]+\exp\left[-j\left(\frac{t^3}{3}+st\right)\right]\right\}\exp(-jKs)dsdt$$
$$= \frac{1}{2\pi}\int_0^{\infty}\int_{-\infty}^{\infty}\left\{\exp\left[j\left(\frac{t^3}{3}+st-Ks\right)\right]+\exp\left[-j\left(\frac{t^3}{3}+st+Ks\right)\right]\right\}dsdt$$
$$= \frac{1}{2\pi}\int_0^{\infty}\exp\left(j\frac{t^3}{3}\right)\int_{-\infty}^{\infty}\exp\left[js(t-K)\right]dsdt$$
$$+\frac{1}{2\pi}\int_0^{\infty}\exp\left(-j\frac{t^3}{3}\right)\int_{-\infty}^{\infty}\exp\left[-js(t+K)\right]dsdt \quad \text{(A.5)}$$

$$= \frac{1}{2\pi}\int_0^{\infty} \exp\left(j\frac{t^3}{3} \right) 2\pi\delta(t-K)dt + \frac{1}{2\pi}\int_0^{\infty} \exp\left(-j\frac{t^3}{3} \right) 2\pi\delta(t+K)dt$$

$$= \exp\left(\frac{j}{3}K^3 \right)$$

$$= \exp\left[\frac{j}{3}(k+ja)^3 \right]$$

$$= \exp\left(-ak^2\right)\exp\left[\frac{j}{3}\left(k^3 - 3a^2k - ja^3\right) \right].$$

A.3. Reason for using the same phase mask to all CASES in experiments

In the *CASE* I and the *CASE* III, the phase has three terms $[\exp\left(\frac{i}{3}\left(k^3 - 3a^2k - ia^3\right) \right)]$ and there is only one term $[\exp\left(\frac{i}{3}k^3 \right)]$ in the *CASE* II. These higher-order terms are included in calculations of the *CASE* I and the *CASE* II. But I use the k^3 phase mask only to all *CASES* in experiments. This is because I assumed that higher-order phase terms $[\exp\left(\frac{i}{3}(-3a^2k - ia^3) \right)]$ can be ignored due to the relatively small constant *a*. To check the effect of higher-order phase terms, I analyzed propagation dynamics of finite power Airy beams generated by a Gaussian beam and an inverse Gaussian beam except higher-order phase terms shown in Figs A1.1(a) and A1.1(b), respectively. They show the exactly same propagation dynamics as Figs. 2.1(a) and 2.1(c), respectively. Therefore, it is confirmed that my assumption is valid.

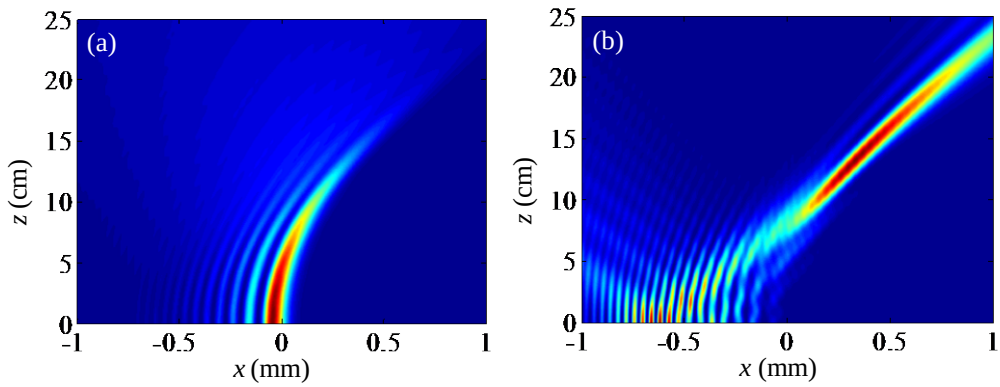

Figure A1.1 Propagation dynamics of finite power Airy beams generated by (a) a Gaussian beam and (b) an inverse Gaussian beam except higher-order phase terms.

Bibliography

1. M. V. Berry and N. L. Balazs, “Nonspreading wave packets,” Am. J. Phys. **47**, 264-267 (1979).

2. G. A. Siviloglou and D. N. Christodoulides, “Accelerating finite energy Airy beams,” Opt. Lett. **32**, 979-981 (2007).

3. G. A. Siviloglou, J. Broky, A. Dogariu, and D. N. Christodoulides, “Observation of accelerating Airy beams,” Phys. Rev. Lett. **99**, 213901 (2007).

4. J. Baumgartl, M. Mazilu, and K. Dholakia, “Optically mediated particle clearing using Airy wavepackets,” Nature Photon. **2**, 675-678 (2008).

5. J. Broky, G. A. Siviloglou, A. Dogariu, and D. N. Christodoulides, “Self-healing properties of optical Airy beams,” Opt. Express **16**, 12880-12891 (2008).

6. H. Raether, Surface Plasmons on Smooth and Rough Surfaces and on Gratings (Springer-Verlag, 1988).

7. W. L. Barnes, A. Dereux, and T. W. Ebbesen, “Surface plasmon subwavelength optics,” Nature **424**, 824-830 (2003).

8. J. A. Schuller, E. S. Barnard, W. Cai, Y. C. Jun, J. S. White, and M. L. Brongersma, “Plasmonics for extreme light concentration and manipulation,” Nature mater. **9**, 193-204 (2010).

9. E. Verhagen, A. Polman, and L. K. Kuipers, “Nanofocusing in laterally tapered plasmonic waveguides,” Opt. Express **16**, 45-57 (2008).

10. T. Thio, K. M. Pellerin, R. A. Linke, H. J. Lezec, and T. W. Ebbesen, “Enhanced light transmission through a single subwavelength aperture,” Opt. Lett. **26**, 1972-1974 (2001).

11. M. I. Stockman, “Nanofocusing of optical energy in tapered plasmonic waveguides,” Phys. Rev. Lett. **93**, 137404 (2004).

12. S. I. Bozhevolnyi, V. S. Volkov, E. Devaux, J.-Y. Laluet, and T. W. Ebbesen, "Channel plasmon subwavelength waveguide components including interferometers and ring resonators," Nature **440**, 508-511 (2006).

13. O. Nicoletti, F. de la Peña, R. K. Leary, D. J. Holland, C. Ducati, and P. A. Midgley, "Three-dimensional imaging of localized surface plasmon resonances of metal nanoparticles," Nature **502**, 80-84 (2013).

14. T. R. Jensen, M. D. Malinsky, C. L. Haynes, and R. P. V. Duyne, "Nanosphere Lithography: Tunable Localized Surface Plasmon Resonance Spectra of Silver Nanoparticles," J. Phys. Chem. B. **104**, 10549-10556 (2000).

15. J. N. Anker, W. P. Hall, O. Lyandres, N. C. Shah, J. Zhao, and R. P. V. Duyne, "Biosensing with plasmonic nanosensors," Nature Mater. **7**, 442-453 (2008).

16. X. Zhang and Z. Liu, "Superlenses to overcome the diffraction limit," Nature Mater. **7**, 435-441 (2008).

17. I. I. Smolyaninov, Y.-J. Hung, C. C. Davis, "Magnifying Superlens in the Visible Frequency Range," Science **23**, 1699-1701 (2007).

18. Z.-W. Liu, Q.-H. Wei, and X. Zhang, "Surface plasmon interference nanolithography," Nano lett. **5**, 957-961 (2005).

19. P. Zijlstra, J. W. M. Chon, and M. Gu, "Five-dimensional optical recording mediated by surface plasmons in gold nanorods," Nature **459**, 410-413 (2009).

20. N. Fang, H. Lee, C. Sun, X. Zhang, "Sub-Diffraction-Limited Optical Imaging with a Silver Superlens," Science **308**, 534-537 (2009).

21. A. Salandrino and D. N. Christodoulides, "Airy plasmon: a nondiffracting surface wave," Opt. Lett. **35**, 2082-2084 (2010).

22. A. Minovich, A. E. Klein, N. Janunts, T. Pertsch, D. N. Neshev, and Y. S. Kivshar, "Generation and near-field imaging of Airy surface plasmons," Phys. Rev. Lett. **107**, 116802 (2011).

23. L. Li, T. Li, S. M. Wang, C. Zhang, and S. N. Zhu, "Plasmonic Airy Beam Generated by In-Plane Diffraction," Phys. Rev. Lett. **107**, 126804 (2011).

24. W. Liu, D. N. Neshev, I. V. Shadrivov, A. E. Miroshnichenko, and Y. S. Kivshar, "Plasmonic Airy beam manipulation in linear optical potentials," Opt. Lett. **36**, 1164-1166 (2010).

25. P. Zhang, S. Wang, Y. Liu, X. Yin, C. Lu, Z. Chen, and X. Zhang, “Plasmonic Airy beams with dynamically controlled trajectories,” Opt. Lett. **36**, 3191-3193 (2010).

26. K.-Y. Kim, C.-Y. Hwang, and B. Lee, “Slow non-dispersing wavepackets,” Opt. Express **19**, 2286-2293 (2011).

27. Y. Lim, S.-Y. Lee, K.-Y. Kim, J. Park, and B. Lee, “Negative refraction of Airy plasmons in a metal-insulator-metal waveguide,” IEEE Photon. Tech. Lett. **23**, 1258-1260 (2011).

28. A. E. Klein, A. Minovich, M. Steinert, N. Janunts, A. Tünnermann, D. N. Neshev, Y. S. Kivshar, and T. Pertsch, “Controlling plasmonic hot spots by interfering Airy beams,” Opt. Lett. **37**, 3402-3404 (2012).

29. T. Ellenbogen, N. Voloch-Bloch, A. Ganany-Padowicz, and A. Arie, “Nonlinear generation and manipulation of Airy beams,” Nat. Photon. **3**, 395-398 (2009).

30. I. Dolev, T. Ellenbogen, N. Voloch-Bloch, and A. Arie, “Control of free space propagation of Airy beams generated by quadratic nonlinear photonic crystals,” Appl. Phys. Lett. **95**, 201112 (2009).

31. I. Dolev, T. Ellenbogen T, and A. Arie, “Switching the acceleration direction of Airy beams by a nonlinear optical process,” Opt. Lett. **35**, 1581-1583 (2010).

32. P. Polynkin, M. Kolesik, J. V. Moloney, G. A. Siviloglou, and D. N. Christodoulides, “Curved plasma channel generation using ultraintense Airy beams,” Science **324**, 229-232 (2009).

33. N. Voloch-Bloch, Y. Lereah, Y. Lilach, A. Gover, and A. Arie, “Generation of electron Airy beams,” Nature **494**, 331-335 (2013).

34. D. Choi, I.-M. Lee, J. Jung, J. Park, J. -H. Han, and B. Lee, “Metallic-Grating-Based Interconnector Between Surface Plasmon Polariton Waveguides,” J. Lightwave Technol. **494**, 331-335 (2013).

35. Y. Jiang, K. Huang, and X. Lu, “Airy-related beam generated from flat-topped Gaussian beams,” J. Opt. Soc. Am. A **29**, 1412-1416 (2012).

36. S. Barwick, “Reduced side-lobe Airy beams,” Opt. Lett. **36**, 2827-2829 (2011).

37. J. D. Ring, C. J. Howls, and M. R. Dennis, “Incomplete Airy beams: finite energy from a sharp spectral cutoff,” Opt. Lett. **38**, 1639-1641 (2013).

38. D. Choi, K. Lee, K. Hong, I.-M. Lee, K.-Y. Kim, and B. Lee, “Generation of finite power Airy beams via initial field modulation,” Opt. Express, **21**, 18797-18804 (2013).

39. D. N. Christodoulides, “Optical trapping: riding along an Airy beam,” Nature Photon. **2**, 652-653 (2008).

40. Z. Zheng, B.-F. Zhang, H. Chen, J. Ding, and H.-T. Wang, “Optical trapping with focused Airy beams,” Appl. Opt. **50**, 43-49 (2011).

41. P. Zhang, J. Prakash, Z. Zhang, M. S. Mills, N. K. Efremidis, D. N. Christodoulides, and Z. Chen, “Trapping and guiding microparticles with morphing autofocusing Airy beams,” Opt. Lett. **36**, 2883-2885 (2011).

42. J. Baumgartl, G. M. Hannappel, D. J. Stevenson, D. Day, M. Gu, and K. Dholakia, “Optical redistribution of microparticles and cells between microwells,” Lab Chip **9**, 1334-1336, (2009).

43. A. Ashkin, J. M. Dziedzic, J. E. Bjorkholm, and S. Chu, “Observation of a single-beam gradient force optical trap for dielectric particles,” Opt. Lett. **11**, 288-290 (1986).

44. J. Baumgartl, G. M. Hannappel, D. J. Stevenson, D. Day, M. Gu, and K. Dholakia, “Optical redistribution of microparticles and cells between microwells,” Lab Chip **9**, 1334-1336 (2009).

45. A. Ashkin, “History of optical trapping and manipulation of small-neutral particle, atoms, and molecules,” IEEE J. Sel. Top. Quantum Elec. **6**, 841-856 (2000).

46. D. G. Grier, “A revolution in optical manipulation,” Nature **424**, 810-816 (2003).

47. J. Liesener, M. Reicherter, T. Haist, and H. J. Tiziani, “Multi-functional optical tweezers using computer-generated holograms,” Opt. Commun. **185**, 77-82 (2000).

48. J. E. Curtis, B. A. Koss, D. G. Grier, “Dynamic holographic optical tweezers,” Opt. Commun. **207**, 169-175 (2002).

49. D. Choi, K. Hong, K. Lee, J. Cho, I.-M. Lee, and B. Lee, “Airy beam generation based on holographic recording and reconstruction,” in OSA Topical Meeting on Digital Holography and Three-Dimensional Imaging, (Optical Society of America, 2013), paper DW2A21.

50. D. Choi, Y. Lim, I.-M. Lee, S. Roh, and B. Lee, “Airy beam excitation using a subwavelength metallic slit array,” IEEE Photon. Tech. Lett. **24**, 1440-1442 (2012).

51. J. Durnin, J. J. Micely Jr., and J. H. Eberly, “Diffraction-free beams,” Phys. Rev. Lett. **99**, 1499-1501 (1987).

52. M. A. Bandres, J. C. Gutiérrez-Vega, and S. Chávez-Cerda, “Parabolic nondiffracting optical wave fields,” Opt. Lett. **29**, 44-46 (2004).

53. J. Hahn, H. Kim, and B. Lee, “Optimization of the spatial light modulation with twisted nematic liquid crystals by a genetic algorithm,” Appl. Opt. **47**, D87-D95 (2008).

54. X.-Z. Wang, Q. Li, and Q. Wang, “Arbitrary scanning of the Airy beams using additional phase grating with cubic phase mask,” Appl. Opt. **51**, 6726-6731, (2012).

55. J. Goodman, Introduction to Fourier Optics, 3rd ed. (Roberts & Company, 2005).

56. M.-L. Hsieh and K. Y. Hsu, “Grating detuning effect on holographic memory in photopolymers,” Opt. Eng. 4**0**, 2125-2133 (2001).

57. G. A. Siviloglou, J. Broky, A. Dogariu, and D. N. Christodoulides, “Ballistic dynamics of Airy beams,” Opt. Lett. **33**, 207-209 (2008).

58. H. I. Sztul and R. R. Alfano, “The Poynting vector and angular momentum of Airy beams,” Opt. Express, **16**, 9411-9416 (2008).

59. C.-Y. Hwang, D. Choi, K.-Y. Kim, and B. Lee, “Dual Airy beam,” Opt. Express **18**, 23504-23516 (2010).

60. P. Rose, F. Diebel, M. Boguslawski, and C. Denz, “Airy beam induced optical routing,” Appl. Phys. Lett. **102**, 101101 (2013).

61. H. F. Shi, C. T. Wang, C. L. Du, X. G. Luo, X. C. Dong, and H. T. Gao, “Beam manipulating by metallic nano-slits with variant widths,” Opt. Express **13**, 6815-6820 (2005).

62. D. Choi, Y. Lim, S. Roh, I.-M. Lee, J. Jung, and B. Lee, “Optical beam focusing with a metal slit array arranged along a semicircular surface and its optimization by genetic algorithm,” Appl. Opt. **49**, A30-A35 (2010).

63. Z. Liu, J. M. Steele, W. Srituravanich, Y. Pikus, C. Sun, and X. Zhang, “Focusing surface plasmons with a plasmonic lens,” Nano lett. **5**, 1726-1729 (2005).

64. B. Lee, S. Kim, H. Kim, and Y. Lim, “The use of plasmonics in light beaming and focusing,” Prog. Quantum Electron. **34**, 47-87 (2010).

65. H. Kim, J. Park, S.-W Cho, S.-Y Lee, M. Kang, and B. Lee, “Synthesis and dynamic switching of surface plasmon vortices with plasmonic vortex lens,” Nano lett. **10**, 529-536 (2010).

66. J. Park, H. Kim, I.-M. Lee, S. Kim, J. Jung, and B. Lee, “Resonant tunneling of surface plasmon polariton in the plasmonic nano-cavity,” Opt. Express **16**, 16903-16915 (2008).

67. COMSOL Multiphysics, [Online]. Available: http://www.comsol.com

68. E. Palik, Handbook of Optical Constants of Solids (Academic Press, 1985).

69. Q. Cao and P. Lalanne, “Negative role of surface plasmons in the transmission of metallic gratings with very narrow slits,” Phys. Rev. Lett. **88**, 057403 (2002).

70. X. Jiao, P. Wang, L. Tang, Y. Lu, Q. Li, D. Zhang, P. Yao, H. Ming, and J. Xie, “Fabry-Pérot-like phenomenon in the surface plasmons resonant transmission of metallic gratings with very narrow slits,” Appl. Phys. B **80**, 301-305 (2005).

한글 초록

베셀빔, 웨버빔과 같이 대표적인 비회절성 빔 중 하나인 에어리 빔은 진행하면서 필드 분포가 처음의 모양 그대로 유지되는 성질을 갖는다. 이는 자유 입자의 운동을 기술한 슈뢰딩거 방정식의 실용해로서 연구되었으며 최근 실험을 통해서 측정되었다. 이러한 에어리 빔은 크게 세가지 독특한 성질을 가지고 있다. 비회절성은 에어리 빔이 진행하는 동안 횡단방향의 필드가 에어리 필드 형태를 계속해서 유지하는 것을 말한다. 자유 가속은 에어리 빔이 진행할 때 외부의 힘이 가해지지 않았음에도 불구하고 진행방향이 휘는 성질을 보인다. 이는 비회절성 빔 중 오직 에어리 빔에서만 나타나는 독특한 성질이다. 마지막으로 자기 회복은 에어리 빔이 장애물을 만나도 얼마 뒤 처음과 비슷한 필드 분포를 회복하는 성질이다. 이러한 성질은 수 많은 빛 다발이 휘어진 형태의 포락선을 형성하는 것으로 설명할 수 있다. 하지만 수많은 빛 다발을 구현하기는 현실적으로 불가능하기 때문에 에어리 빔을 실제로 만드는데는 다른 방법이 필요하다. 따라서 에어리 빔의 사이드 로브를 제거한 형태인 유한한 에어리 빔이 제안되었다. 이러한 형태의 에어리 빔은 자유 가속, 자기 회복 등의 성질을 가지지만 비회절성질은 시간이 지남에 따라 잃게 된다.

본 논문에서는 입사하는 빔의 필드를 변조함으로써 다향한 형태의 에어리 빔을 만들었다. 특히 평면파를 사용하여 만든 에어리 빔은 가우시안빔으로 만들어진 일반적인 에어리 빔에 비해 비회절성이 향상된 결과를 얻었다. 또, 인버스-가우시안빔으로 만든 에어리 빔은 휘어진 포커스를 형성하는 것을 보였다. 이론 및 실험을 통하여서 입사하는 빔이 에어리 빔에 어떤 영향을 미치는지를 제시하였다.

다음으로 홀로그래피를 이용하여 에어리 빔을 만드는 새로운 방법을 제안하였다. 레퍼런스빔과 에어리 빔의 홀로그램을 기록하고 이를 재생하는 방법으로 복잡한 실험장치 없이 간단하게 에어리 빔을 구현하였다. 레퍼런스빔 전체를 입사하지 않더라도 에어리 빔이 만들어지는 자기 회복을 보였으며, 레퍼런스빔을 반대방향에서 조사함으로써 파워의 방향이 반대인 에어리 빔을 구현하였다. 이는 기존의 공간광변조기를 이용하여서는 구현할 수 없는 것이다. 또, 실제적인 응용을 위해 각다중화를 실험하였다. 이는 동시에 여러개의 입자를 옮기거나 제어할 수 있는 기술이 될 것이라 예상된다.

마지막으로 금속 슬릿 어레이를 이용하여 에어리 빔을 만드는 방법을 제안하였다. 호이겐스의 원리에 따라 표면 플라즈몬이 슬릿을 통과할 때의 파워와 위상을 조절하여 초기 에어리 빔의 강도 및 위상 분포와 같게 만들어주면 에어리 빔이 형성될 수 있음을 보였다. 이는 특별한 광학 장치 없이 매우 작은 구조로 만들 수 있기 때문에 광집적회로에서의 신호전달이나 입자조작과 같은 곳에 응용될 것이라 생각된다.

감사의 글

감사의 글을 쓰려고 돌아보니 6 년간의 대학원 생활이 정말 빠르게 지나간 것 같습니다. 졸업은커녕 논문 한 편은 쓸 수 있을까 했었던 게 엊그제 같은데 저에게도 이런 날이 오긴 하는군요. 연구실에 있는 동안 좋은 선후배님들을 많이 만났고 많은 것을 배웠습니다. 이 지면을 빌어 감사의 마음을 표현하고자 합니다.

먼저 저의 지도 교수님이신 이병호 교수님께 감사를 드립니다. 무지몽매한 저를 지금까지 이끌어주셨고 가르쳐주셨습니다. 늘 한결 같으시며 성실하신 교수님께 많이 배웠고 도전을 받았습니다. 앞으로 사회에 나가서도 교수님의 제자로서 부끄럽지 않은 삶을 살겠습니다.

더불어 부족한 저의 논문을 심사해주신 이신두 교수님, 정윤찬 교수님, 염동일 교수님, 임용준 박사님께 감사를 드립니다. 작은 것 하나까지도 꼼꼼히 연구하는 자세를 배우게 되었고, 제가 조금이나마 발전하게 된 계기가 되었습니다.

저를 잘 챙겨주시고 신경 써주신 정재훈 교수님께 감사를 드립니다. 저의 잘못을 통해 많이 배웠고 성장할 수 있었습니다. 회사에 가서도 사람들의 마음을 잘 이해하는 사람이 되도록 노력하겠습니다. 부족한 저의 연구를 함께 봐주신 김경염 교수님께도 감사를 드립니다. 탁월한 교수님의 가르침으로 제가 논문다운 논문을 쓸 수 있었다고 생각합니다. 늘 민폐만 끼친 것 같아 죄송스러운 마음뿐입니다. 또, 석사와 박사과정 동안 저에게 가장 큰 가르침을 주신 이일민 박사님께도 감사를 드립니다. 귀찮은 내색 전혀 없이 하나하나 알려주시고, 저의 모든 논문을 수정해주시고, 가르침을 주신 일민이형 덕분에 오늘까지 올 수 있었던 것 같습니다. 연구실 생활을 함께하진 못했지만 얼굴을 뵙고 조언을 아끼지 않으셨던 김성철 교수님, 민성욱 교수님, 최희진 교수님, 김정호 교수님, 이용욱 교수님, 박재형 교수님, 한승훈 박사님께도 감사를 드립니다.

사랑하는 광공학 연구실 선후배님들께도 감사를 드립니다. 못하는 것이 없으셨던 준구형, 모르는 것이 없으셨던 휘형, 대구 촌놈을 명동으로 데려가 주신 지수형, 언제 봐도 기분 좋은 윤희누나, 자상하신 주환이형, 저를 졸업시켜 주신 용준이형, 배울 것이 너무 많은 정현이형, 멀리사시는 영민이형, 버릇없는 행동도 다 받아주신 숙영누나, 맥가이버 같은 길배형, 강한 남자 재훈이형, 의리의 재현이형, 정이 많은 성우형, 간지남 진모, 여장부 은희, 나의 동기 능력자

민수, 장난치고 싶은 동호, , 멋지다 잘생긴 인덕이, 기분 좋게 웃는 치영이, 도시 남자 우영이 모두 어디서든지 인정받고 성공하길 기도하겠습니다.

젠틀하신 한식이형, 졸업을 함께한 태린누나, 사.. 사.. 좋아하는 준범이형, 한국말 잘하는 첸니, 연구실의 기둥 승열이, 순수르 순기, 늘 고맙고 미안한 지운이, 전설이 될 방장 의영이, 만능 스포츠맨 강이, 남자로서 매력이 넘치는 종현이, 아이돌 눈망울의 창건이, 반공지 규호, 차기 nature 저자 현수, 후배인데도 배울 것이 많은 규근이, 봐주는 것 없는 준수, 감성있는 엔지니어 재범이, 똘똘한 창원이, 예의 바른 영모, 모델 같은 종영이, 해외파 맷, 친절하게 도와주셨던 지연누나, 늘 최선을 다하는 요한이, 도마 맛 선제, 3D 팀의 새 바람 진수, 마지막으로 6 년 동안 모자란 나를 도와주고 함께한 기훈이형, 폐만 끼치고 갑니다. 모두 좋은 논문 쓰시고 건강하시길 기도하겠습니다.

사랑하는 나의 친구 현우, 좋은 가정 이뤘으니 2 세 소식도 빨리 들려주고 힘든 시기도 있었던 만큼 더 행복했으면 좋겠다. 승리자 영재야, 고생문이 열렸지만 더 행복하겠지? 아기 잘 키우고 돈도 많이 벌길 바란다. 희동아, 얼마 전부터 카톡에 여자친구랑 같이 찍은 사진이 보이던데 잘 돼가는 거지? 빨리 좋은 소식 들려주길 바래.

용규형, 이제 일 그만하고 연애 사업도 하셔야죠? 승오형, 우리는 함께입니다. 대한이형, 재만이형, 부럽네요.. 또르르.. 이제 너무 오래돼서 몇 명 기억나진 않지만 어딘가에서 자기 역할을 하고 있을 충성교회 친구들, 효창이, 인섭이, 태일이, 하은이, 지원이, 지연이, 유미 모두 보고 싶구나. 하는 일 모두 잘 되길 바란다. 박사기간 지친 마음을 위로해준 큰은혜교회 식구들, 모두 감사하고 사랑합니다.

존경하는 아빠, 엄마, 누나. 무뚝뚝한 아들, 동생이 이렇게 졸업을 하게 됐네. 모두 덕분이야. 내가 앞으로 더 잘하도록 노력할께. 우리가족 오래오래 건강하고 더 행복하게 살자.

지금까지 나의 길을 인도하신 하나님, 어느 자리에 있든지 하나님의 영광을 나타내는 자녀가 되도록 살겠습니다. 지켜봐 주세요.

연예인들 수상소감 말하는 기분입니다. 혹시 감사의 글에서 누락된 분은 개인적으로 찾아 뵙고 인사를 드리겠습니다. 모두 감사합니다.

2014 년 2 월 최다운 올림.